A continuum model for heat and mass transfer in moving-bed reactors for thermochemical energy storage

David Korba^{1,‡}, Wei Huang^{1,‡}, Kelvin Randhir², Joerg Petrasch², James Klausner², Nick AuYeung³, and Like Li^{1,*}

- 1. Department of Mechanical Engineering, Mississippi State University, Mississippi State, MS 39762, USA
- 2. Department of Mechanical Engineering, Michigan State University, East Lansing, MI 48824, USA
- 3. School of Chemical, Biological and Environmental Engineering, Oregon State University, Corvallis, OR 97331, USA
- [‡] These authors contributed equally to this work
- * Corresponding author: <u>likeli@me.msstate.edu</u>

Abstract

In this work, a continuum heat and mass transfer model coupling transport phenomena and high-temperature thermochemical reactions is developed for stationary packed-bed and counterflow moving-bed reactors. After presenting the general modeling framework, we focus on the 2D axisymmetric version of the model for which validation is conducted with experimental results for a packed-bed reactor in the literature for manganese-iron oxide reduction/oxidation and an inhouse counter-flow moving-bed reactor for magnesium-manganese oxide reduction up to 1450°C. Transient simulation results including the local distributions of gas/solid temperatures, oxygen concentration and the extent of reaction, as well as the various energy flow components and energy conversion efficiencies are reported. The results based on the 2D axisymmetric model are also compared with those obtained from a previous 1D model. The comparison shows that capturing the radial variation is critical in reactor modeling and the 2D results demonstrate improved agreement with experiments. Specifically, large temperature variations along the radial direction are observed especially in the reaction zone; this non-uniform radial temperature distribution has a significant effect on the chemical reaction extent due to its strong dependence on temperature; and the overall oxygen concentration at the reactor exit and the predicted system efficiency are slightly lower in the 2D model compared to the 1D model. The present heat and mass transfer model can provide valuable insights into reactor design, scale-up, and operating conditions selection to maximize system energy storage efficiency.

Keywords: thermochemical energy storage; counter-flow direct heat transfer; moving-bed reactor; thermal reduction; axisymmetric model.

Nomenclature			
Latin letters			
$a_{\rm gs}$	interstitial specific surface area	ϵ	minimum velocity convergence residual
$A_{ m W}$	surface area of reactor heated zone	ε	bed porosity
$c_{\rm p}$	heat capacity	$\mathcal{E}b$	bulk porosity
C	concentration of species	$\mathcal{E}_{\mathrm{por}}$	intra-particle porosity
D	diffusivity	η^{\cdot}	molar flow rate
$d_{ m p}$	particle diameter	$\eta_{ m furnace}$	electrical to chemical efficiency
e	emissivity	$\eta_{ m pump}$	pump efficiency
Ė _{chem}	rate of chemical energy stored	$\eta_{ m sep}$	separation efficiency
G	mass velocity	$\eta_{ m system}$	total energy input-to-chemical efficiency
$h_{ m amb}$	wall-to-ambient heat transfer coefficient	$\eta_{ m tc}$	thermal input-to-chemical thermochemical efficiency
$h_{ m gs}$	heat transfer coefficient between gas and	κ_D	permeability of the bed
	solid phases	ND	drag parameter describing inertial
$h_{ m gw}$	gas-to-wall convective heat transfer	κ_E	effects
ngw	coefficient	λ	ratio of power entering reactor to total electric input power
,	solid-to-wall effective radiative heat	μ	dynamic viscosity
h_r	transfer coefficient	ξ	mass fraction
	wall-to-ambient effective radiative heat	-	
$h_{\rm rw}$	transfer coefficient	ρ	density
h_{sw}	solid-to-wall convective heat transfer coefficient	σ	Stefan-Boltzmann constant
h_w	wall-to-ambient heat transfer coefficient		
k	thermal conductivity	Subscripts	
m	mass	avg	average
m	mass flow rate	ь	bulk
p	pressure	eff	effective
Pe	Peclet number	f-a	furnace-to-ambient
$P_{ m electric}$	electric power supplied to furnace	g	gas phase
$\dot{P}_{ m pump}$	power required to move gas through bed	in	inlet
Pr	Prandtl number	mid	midline
q_w	heat flux on reactor wall	out	outlet
· .	power removed on outside of reactor	ox	oxidized
$Q_{ m loss}$	wall	p	particle
$\dot{Q}_{O2,\mathrm{sep}}$	power required to separate O ₂ from N ₂	red	reduced
202,sep	rate of sensible heat absorbed by	rea	reduced
$Q_{ m sens,s/g}$	solid/gas	S	solid phase
$\dot{Q}_{ m sens,w}$	rate of sensible heat absorbed by reactor tube wall	W	wall
r_{0_2}	species production rate per unit volume		
R	universal gas constant		
Re	Reynold's number		
t	time	Abbreviations	
T	temperature operational temperature of the solid	ADI	alternating-direction implicit
T_{sep}	oxide separation membrane	BC	boundary condition
u	velocity	CSP	concentrated solar power
V	volume	FD	finite difference
\dot{V}	volume flow rate	HTF	heat transfer fluid
\dot{V}	volume flow rate	PCM	phase-change material
		PDA	pentadiagonal algorithm
Greek letters		PV	photovoltaic

α	extent of reaction	QUDS	quadratic, upstream-weighted finite difference scheme
γ	mole fraction	SLPM	standard liter per minute
ΔH	enthalpy change per unit molar oxygen	TCES	thermochemical energy storage
ΔP_{avg}	average pressure drop across bed	TDA	tridiagonal algorithm
Δt	time step	TES	thermal energy storage

I. Introduction

There has been great interest and technological advancement in integrating novel energy storage concepts with renewable power generation to resolve their intermittent and variable nature. Some common methods of generating power from renewable sources include concentrated solar power (CSP), photovoltaic (PV), and wind generated power. Thermal energy storage (TES) is particularly attractive as CSP is typically directly used as heat input, while both PV and wind can be used to power an electric furnace for TES. TES methods typically fall into one of three domains: (1) sensible energy storage – thermal energy is stored in a large high-heat capacity aggregate in the form of sensible heat, (2) *latent heat storage* – generated energy is stored in the form of latent heat in a phase-change material (PCM), and (3) thermochemical energy storage (TCES) generated heat is converted into a *chemical potential energy* through an endothermic reaction step and later reversed through an exothermic oxidation step to generate thermal energy when needed [1]. For sensible heat and latent heat storage systems, the maximum achievable energy densities range near 1.5-1.8 GJ/m³ with maximum temperatures near 800-900°C [2-4]. In comparison, TCES demonstrates energy storage densities above 3 GJ/m³ with temperatures as high as 1500°C [2,5]. High energy storage density, high operating temperatures, and the excellent long-duration (even seasonal) storage capability of TCES has encouraged significant research in this field in recent years.

As expected, a large focus of recent work has been numerically and experimentally studying different thermochemical reactor designs/concepts and TCES materials [6–9]. Several reactor concepts have been proposed, typically falling into different categories such as those with (1) fixed or continuous operation, (2) packed bed, fluidized beds, moving/falling particle beds, etc., and (3) direct or indirect heat transfer. Specifically, this paper focuses on the numerical modeling of a tubular reactor with a moving bed and a counter-current gas flow as the heat transfer fluid (HTF).

While we are concerned with moving beds for TCES within this paper, certain numerical modeling concepts are consistent between both packed beds (both TCES and sensible heat storage) and moving particle beds, thus we find it instrumental to discuss these models here. The interested

reader is referred to [6,10–17] for further discussions concerning fluidized beds for TCES. Several packed bed models have been proposed and validated with laboratory-scale experiments. Meier et al. performed an experimental and numerical analysis on a 0.15 m diameter packed bed of magnesium silicate spherical particles for sensible energy storage [18]. Mertens et al. presented a 1D two-phase thermal non-equilibrium approach, validating their model against the experiment in Meier et al. [19]. Anderson et al. performed an analysis on a packed bed of alpha-alumina utilizing compressed air as the HTF, noting that care should be taken in the determination of the gas-tosolid heat transfer coefficient and that the use of thermally-dependent physical properties plays a large role in simulation accuracy [20]. Their model was presented through the use of dimensionless parameters and radial effects were assumed negligible; thus the model was one-dimensional. Bayon and Rojas used a dimensionless single phase 1D model to study the effects of a "real-size" thermocline tank [21]. Zanganeh et al. experimentally studied a 6.5 MWh pilot-scale packed bed reactor, presenting a corresponding two-phase 1D model which was used to simulate a 7.2 GWh industrial scale reactor after validation [22]. The same group further studied operational and design parameters with the proposed 1D model, presenting key interest variables such as thermal losses and overall efficiency [23]. Preisner et al. presented a 1D two-phase moving bed model, also considering mass balance and species transport to simulate a moving particle bed for TCES [24]. They validated their model with an experimental reactive packed bed with manganese iron-oxide as the TCES material [25,26].

While the above models and others differ in material, size, operational implementation, etc., it is obvious that the 1D modeling approach is a common assumption for packed beds and moving beds presented in literature. While 1D models provide a simple and computationally efficient method for modeling such reactors, a detailed analysis on non-axial variations (2D/3D) with tube-style reactors is worthwhile, with some key references already noting observable variations for similar designs. While we are focused on TCES, tubular counter-current flow reactor designs have been used in other industries, one namely of interest is the reduction of hematite in the iron-making process. A 1D pellet model was studied by Negri et al. for a counter-current style reactor for hematite [27]. Valipour and Saboohi further presented a 2D axisymmetric model for a similar reactor design [28]. Their results demonstrate that deviations in key parameters such as temperature and percent of conversion can be observed in the radial direction of the cylindrical design. In the study of PCM and sensible heat storage, Ismail and Stuginsky presented a detailed

study on fixed bed designs for both concepts, also directly comparing simulations from both 1D and 2D models [29]. Overall, their study showed that deviations were present between the two, however they appeared negligible for the reactor and were not a large focus of the study. A 1.55 MWh packed bed design for sensible energy storage was numerically studied with a 2D model by Klein et al. with validation to experimental data [30]. They demonstrated large radial variations within the fixed bed during transient portions of their experiment/simulation, approaching difference values near 200°C at specific bed heights during the 6 h operation window. Furthermore, a recent 2D packed bed model by Hamidi et al. for TCES with iron-manganese oxides also demonstrates radial disparities in certain regimes of their reactor [31]. A similar reactor design for methane reforming with carbon dioxide was simulated by Lu et al. [32]. Within their study, they further observed variation in temperature and flow velocity in the radial direction of the tube, especially near the reactor wall where heating occurred. Wang et al. presented a 3D model for a parallel flow moving bed design for TCES, considering the full-reactor setup with a single tube [2]. Their study showed obvious variation in the azimuthal direction, however radial effects were not discussed within their study. The same group also presented a packed bed model for TCES with iron-manganese oxide particles for a similar reactor design, demonstrating a maximum temperature difference of 214.8°C in the azimuthal direction [33]. While not a tubular design, Schrader et al. discussed a moving bed for aluminum-doped calcium manganite [34,35]. Their design, instead, controlled particle flow rate through the inclination angle in a gravity-fed tilt bed concept, and the demonstrated temperature plots of the reactor cavity surface show an apparent difference in all directions within the reactor. It is obvious from these models that variations in different directions of the reactor could be present depending on the reactor design and operating conditions. Hence a general multi-dimensional modeling framework is desired.

This paper aims to develop a coupled multi-dimensional heat and mass transfer model for high-temperature thermochemical reactions in tubular reactors with stationary or moving-bed configurations. The detailed simulation results are presented in 2D, but the governing equations and numerical methodology are directly applicable to 3D. The major novelties of the present model include: (1) a novel strategy for solving the momentum equation for porous media flow is proposed through a pressure-correction method, which is easily extendable to 3D porous media flows, unlike previous 1D uniform or plug flow assumptions or stream-function formulations [28,36–38] that are mainly applicable to 2D; (2) the current work primarily considers a redox reaction within Mg-

Mn-O particles at elevated operating temperatures up to 1500°C. Thus, the current model considers temperature dependent material parameters that are updated within each time step and can be used for future redox reactions with similar high operating temperatures; (3) detailed simulation results are presented and the present model is validated in terms of long-time temperature and reaction yield measurements with past literature [26] for a stationary packed-bed reactor (tube ID 54.3 mm, length 195 mm and experiment time 250 min) as well as the in-house experimental data [39] from a moving-bed reactor (tube ID 50.8 mm, length 1420 mm and experiment time 180 min); (4) both transient and steady energy flow components are recorded in our model and high thermochemical and system energy conversion efficiencies are predicted at steady state ($\eta_{tc} \sim 95\%$ and η_{system} between 25%-30%), which agree with those based on measurements in [39]; and (5) a parametric study is also performed to illustrate the radial temperature and extent-of-reaction variations for different reactor sizes and demonstrate the improvement of the 2D model over the previous 1D model in [40].

The rest of this paper is arranged as follows: Section II presents the model assumptions, governing equations, boundary conditions, and solution procedures used to simulate the countercurrent flow reactor. Section III-A validates the model with reported results for a stationary packed-bed reactor, and Sect. III-B validates the model with our own experimental data for a moving-bed reactor. A detailed energy budget and conversion efficiency analysis is then presented in Sect. III-C and the influence of varied reactor tube diameters is studied in Sect. III-D to highlight the advantages of the multi-dimensional model. And Section IV concludes the paper. Comparisons between the 1D and 2D axisymmetric models are discussed within each section.

II. Model Description

This work utilizes a transient finite-difference (FD) method to simulate the coupled transport-reaction in high-temperature moving particle-bed reactors. The gas and solid phases are considered at the continuum scale in thermal non-equilibrium [41] and are coupled through a convective term. Temperature dependency is considered for the key material properties which are updated at the end of each time step. A 2D slice of the considered reactor design for this model is schematically depicted in **Figure 1**, with gas flow entering at the bottom, solid particle flow entering at the top, and heat being applied in the middle reactor regime. It is noted that an electric furnace is depicted in **Figure 1** to provide heat to fuel the reaction for the experimental setup, but

a working design would instead use CSP to generate the needed thermal energy. The corresponding model is based on the following assumptions:

- 1. The ideal gas law is applicable to the gases (both gas mixture and the released oxygen alone).
- 2. Ergun's equation is used to link the pressure drop in the moving bed to the gas velocity.
- 3. Mono-dispersed particles with homogenous distribution are assumed; thus they can be treated on the continuum scale.
- 4. The solid particles are moving in the axial direction only with an averaged uniform velocity determined by the solid flow rate.
- 5. The solid particle porosity and bed porosity are both considered constant and not varying with position, temperature, or change between oxidized and reduced states.

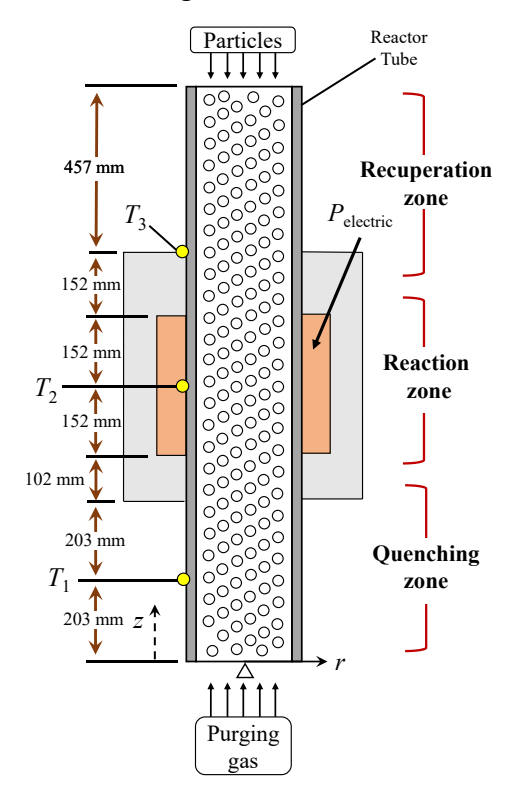


Figure 1: Schematic of the studied moving bed reactor design. The measured temperatures T_1 , T_2 , and T_3 during experiments will be used for model validation.

A. Mass Transfer

All governing equations are presented in vector form, beginning with mass conservation of the gas phase as [42]

$$\frac{\partial \left(\varepsilon \rho_{g}\right)}{\partial t} + \nabla \cdot \left(\rho_{g} \mathbf{u}_{g}^{s}\right) = \nabla \cdot \left(D_{g} \nabla \rho_{g}\right) - (1 - \varepsilon) r_{O_{2}} \tag{1}$$

where ε is the bed porosity, ρ_g the gas density, D_g the gas mixture self-diffusivity, r_{O_2} is the oxygen production rate per unit volume, and \mathbf{u} denotes the velocity; the g and g subscripts refer to the gas and solid phases, respectively, and the g superscript refers to the superficial velocity. The oxygen production rate is defined as

$$r_{\rm O_2} = -(\rho_{\rm ox} - \rho_{\rm red}) \frac{d\alpha}{dt}, \tag{2}$$

in which ρ_{ox} and ρ_{red} are the respective densities of reference oxidized and reduced materials. In this work, reaction conversion α can be obtained from the mass m of the metal oxide mixture by

$$\alpha = \frac{m - m_{\text{red}}}{m_{\text{ox}} - m_{\text{red}}},\tag{3}$$

with m_{ox} and m_{red} indicating the mass in the reference oxidized and reduced states, respectively. The redox reactions used for validation and comparison in the current work are given in Sect. III-A and Sect. III-B.

B. Momentum Equation

The momentum equation is considered for the gas phase through Ergun's equation [43]:

$$-\frac{\kappa_D}{\mu} \nabla p = \mathbf{u}_g^s + \frac{\rho_g}{\mu} \kappa_E \mathbf{u}_g^s \left| \mathbf{u}_g^s \right| \tag{4}$$

where μ is the dynamic viscosity, κ_D the permeability of the bed and κ_E a drag parameter describing the inertial effect that can be expressed as

$$\kappa_D = \frac{d_p^2 \varepsilon^2}{150(1-\varepsilon)^2}, \ \kappa_E = \frac{1.75d_p}{150(1-\varepsilon)}$$
 (5)

It is pointed out by some authors [24,41] that for sufficiently low Reynold's numbers, Eq. (4) reduces to Darcy's law: $\nabla p = -\mu \mathbf{u}_g^s / \kappa_D$. For 1D modeling, the implementation of Eq. (4) can be realized through coupling the mass transfer and gas energy balance through the ideal gas law and Ergun's equation.

However, for 2D/3D models, the velocity can no longer be treated as a scalar field and instead requires separate treatment to solve the pressure drop-velocity equations. In previous literature [28,36,37], this has typically been done by introducing a stream function. However, the

use of a stream function complicates the boundary conditions and is typically limited to a constant pressure assumption on open-flow boundaries [38]. Therefore, we instead propose to solve Eq. (4) and Eq. (1) through a pressure correction method. Following a related work by Kränzien and Jin [44] for buoyancy driven convection based on Darcy's law, we decompose the pressure as $p = \hat{p} + p'$, thus rewriting Eq. (4) as:

$$-\frac{\kappa_D}{\mu} (\nabla \hat{p} + \nabla p') = \mathbf{u}_g^s + \frac{\rho_g}{\mu} \kappa_E \mathbf{u}_g^s |\mathbf{u}_g^s|$$
(6)

The solution procedure for the pressure and velocity fields are as follows. First, an initial pressure field, \hat{p} , is guessed to find a velocity field that satisfies the momentum equation (in both r- and z- directions) through Eq. (4). Next, Eq. (6) is rearranged to solve for the mass velocity ($\mathbf{G} = \rho_g \mathbf{u}_g^s$):

$$\mathbf{G} = -\frac{\kappa_D \rho_g}{\mu + \kappa_E |\mathbf{G}|} (\nabla \hat{p} + \nabla p')$$
(7)

Eq. (7) is inserted into the steady state continuity equation, resulting in

$$\nabla \cdot \left(\frac{-\kappa_D \rho_g}{\mu + \kappa_E |\mathbf{G}|} (\nabla \hat{p} + \nabla p') \right) = -(1 - \varepsilon) r_{o_2}.$$
 (8)

Eq. (8) is then solved for a corrector pressure, p', and the total pressure, p, is subsequently updated. It is noted that the $|\mathbf{G}|$ term is treated as a known scalar field in Eq. (8). At this point, the resultant pressure satisfies continuity and are used to update the velocity field through Eq. (4). The resulting velocity field will satisfy the momentum equation; however, the pressure field will no longer satisfy continuity. Therefore, p is again set equal to the provisional pressure field, \hat{p} , and the above process is iterated until both the velocity and pressure residuals between iterations reach a convergence threshold, upon which both the continuity and momentum equations are considered simultaneously satisfied.

C. Species Transport

Since O_2 is released/absorbed during the reaction of interest and an O_2 partial pressure dependency is considered in the reaction kinetics, the O_2 species transport is resolved as

$$\varepsilon \rho_{g} \frac{\partial \xi_{O_{2}}}{\partial t} + \rho_{g} \mathbf{u}_{g}^{s} \cdot \nabla \xi_{O_{2}} = \nabla \cdot \left(\rho_{g} D_{O_{2} - N_{2}} \nabla \xi_{O_{2}} \right) - \left(1 - \varepsilon \right) \left(1 - \xi_{O_{2}} \right) r_{O_{2}} \tag{9}$$

where ξ is the mass fraction and $D_{{\rm O_2-N_2}}$ is the diffusivity between ${\rm O_2}$ and ${\rm N_2}$. For the solution of the species transport, Eq. (1) and Eq. (9) are cast together with the scalar of interest instead being the concentration of oxygen $C_{{\rm O_2}} \equiv \rho_{\rm g} \xi_{{\rm O_2}}$:

$$\varepsilon \frac{\partial C_{O_2}}{\partial t} + \nabla \cdot \left(C_{O_2} \mathbf{u}_g^s \right) = \nabla \cdot \left(D_{O_2} \nabla C_{O_2} \right) - \nabla \cdot \left(D_{O_2} \frac{C_{O_2}}{\rho_g} \nabla \rho_g \right) + r_{O_2}$$
(10)

D. Energy Balance

The non-equilibrium gas and solid energy equations are written as [24,41]

$$\left(\varepsilon \rho_{g} c_{p,g}\right) \frac{\partial T_{g}}{\partial t} + \left(\rho_{g} c_{p,g} \mathbf{u}_{g}^{s}\right) \cdot \nabla T_{g} = \nabla \cdot \left(\varepsilon_{b} k_{g} \nabla T_{g}\right) + h_{gs} a_{gs} \left(T_{s} - T_{g}\right)$$

$$\tag{11}$$

and

$$(1-\varepsilon)\rho_{s}c_{p,s}\frac{\partial T_{s}}{\partial t} + \left(\rho_{s}c_{p,s}\mathbf{u}_{s}\right)\cdot\nabla T_{s} = \nabla\cdot\left(k_{s,\text{eff}}\nabla T_{s}\right) + h_{gs}a_{gs}\left(T_{g} - T_{s}\right) + (1-\varepsilon)r_{O_{2}}\Delta H$$

$$(12)$$

where T_g and T_s are the volume-averaged temperatures, ΔH is the enthalpy change per unit molar oxygen, k_g is the thermal conductivity of the gas, and $k_{s,eff}$ is the effective thermal conductivity of the solid particles. In principle, ΔH is dependent on the local temperature, pressure and extent of reaction such as that in [45,46]. A convenient strategy is to assume an averaged constant value of ΔH and consider those dependences in the r_{o_2} term only in Eq. (12). This approximation has been adopted in several previous TCES models [24,25,31,34,35,47] and is also used in the present work. For the material of interest (Mg-Mn-O), ΔH is specified as the enthalpy of reaction for the sample with an Mn/Mg molar ratio of 1:1 and cycling between 1000 and 1500°C for thermochemical reactions, i.e., $\Delta H = 380$ kJ/mol of O₂ [40,48]. Details for the determination of convective heat transfer coefficient h_{gs} can be found in [49]. The interstitial specific surface area is provided as $a_{gs} = 6(1-\varepsilon_b)/d_p$ with d_p being the particle diameter and ε_b the bulk porosity. In order to consider sensible heat storage within the reactor tube (**Figure 1**) and heat loss due to natural convection, transient heat conduction within the tube wall is considered as

$$\left(\rho_{w}c_{p,w}\right)\frac{\partial T_{w}}{\partial t} = \nabla \cdot \left(k_{w}\nabla T_{w}\right) \tag{13}$$

It should be noted that the radial variation through the thin tube wall is neglected and T_w should be considered the average temperature at each axial location.

E. Boundary Conditions

The boundary conditions for a general reactor design (such as that in a typical CSP field) are typically three-dimensional. For both the model validation and simulations presented in this work, we focus on the comparison with two lab-scale reactors design and operation for which axisymmetry is applicable. Hence the boundary conditions below are for axisymmetric models.

Eq. (14) describes the boundary conditions at the top surface of the reactor. The first four conditions denote the fully developed conditions at the outlet for the gas and tube wall, the fifth the controlled particle inlet temperature, set to room temperature for all simulations, and the last condition represents the outlet pressure set to atmospheric pressure, p_{atm} .

$$\frac{\partial \rho_{g}}{\partial z}\Big|_{\text{out}} = 0; \quad \frac{\partial C_{\text{O}_{2}}}{\partial z}\Big|_{\text{out}} = 0; \quad \frac{\partial T_{g}}{\partial z}\Big|_{\text{out}} = 0; \quad \frac{\partial T_{w}}{\partial z}\Big|_{\text{out}} = 0; \quad T_{s} = T_{s,\text{in}}; \quad p_{g,\text{out}} = p_{\text{atm}}; \quad \text{at } z = H \tag{14}$$

Next, the boundary conditions employed at the bottom of the tube are

$$\rho_{g} = \rho_{g,in}; \ C_{O_{2}} = C_{O_{2},in}; \ T_{g} = T_{g,in}; \ \frac{\partial T_{s}}{\partial \overline{z}} \bigg|_{out} = 0; \ \frac{\partial T_{w}}{\partial \overline{z}} \bigg|_{out} = 0; \ u_{g,in}^{s} = \frac{\dot{m}_{g}}{\rho_{g,in}A}, \ \text{at } z = 0$$
 (15)

where the first three conditions are Dirichlet conditions at the gas inlet. The particle and wall temperatures are assumed as fully developed at the outlet z = 0, and the inlet gas velocity is obtained from the mass flow rate of gas, \dot{m}_g . Axisymmetric boundary conditions are assumed at the center of the tube, such that

$$\frac{\partial \rho_g}{\partial r}\bigg|_{r=0} = \frac{\partial C_{O_2}}{\partial r}\bigg|_{r=0} = \frac{\partial T_g}{\partial r}\bigg|_{r=0} = \frac{\partial T_s}{\partial r}\bigg|_{r=0} = \frac{\partial p}{\partial r}\bigg|_{r=0} = 0$$
(16)

At the reactor inner wall, the gas mixture and O_2 are considered non-penetrative, and a mixed boundary condition is utilized to simulate the energy transfer between the gas/solid phases and the wall:

$$\frac{\partial \rho_{g}}{\partial r}\Big|_{r=R} = \frac{\partial C_{O_{2}}}{\partial r}\Big|_{r=R} = \frac{\partial p}{\partial r}\Big|_{r=R} = 0; k_{g} \frac{\partial T_{g}}{\partial r}\Big|_{r=R} = h_{gw}(T_{w} - T_{g,R}); k_{s,eff} \frac{\partial T_{s}}{\partial r}\Big|_{r=R} = (h_{r} + h_{sw})(T_{w} - T_{s,R})$$
(17)

where h_{gw} , h_r [50], and h_{sw} [51,52] are the gas-to-wall convective heat transfer coefficient, solid-to-wall effective radiative and convective heat transfer coefficients, respectively. Lastly,

convection and radiation losses are considered at the outside of the tube for non-insulated sections by

$$k_{w} \frac{\partial T_{w}}{\partial r} \bigg|_{r=R} = h_{\text{amb}} (T_{\text{amb}} - T_{w})$$
(18)

where h_{amb} is a sum of a natural wall convection term, h_w [53], and radiation coefficient, h_{rw} [54]. A detailed list of the thermally dependent parameters can be found in Appendix A. All temperatures are initially set equal to the ambient temperature. Both applied temperature and applied power input boundary conditions were tested and will be discussed in detail in Sect. III.

F. Numerical Implementation

For efficient numerical implementation, all the governing equations and boundary conditions in the previous sections are non-dimensionalized following the same approach as in the 1D model [40] and they are not presented here for brevity. The convection terms are spatially discretized using a third-order quadratic, upstream-weighted finite-difference scheme (QUDS) [55] and the diffusion terms are resolved with a second-order central-difference scheme. The alternating-direction implicit (ADI) method [56] is used for updating the solutions in 2D. First, the four sets of algebraic equations are solved with a pentadiagonal (PDA) matrix algorithm to obtain the updated scalar quantities in the z-direction at $t + \Delta t/2$. Next, a similar process is implemented in the r-direction, where a tridiagonal (TDA) matrix algorithm is used to update the scalars at the new time step $t + \Delta t$. Then, Eq. (13) is solved to update the tube wall temperature. Equations (4,6) are discretized with a second-order central-difference scheme, and the pressure correction method is applied to update the pressure and velocity field. The corrector pressure field in Eq. (8) is solved with the Gauss-Seidel method. The pressure correction method is considered converged when the maximum velocity residual, $u_{\text{res}} = \max\left[\left(u_{g,z}^{n+1} - u_{g,z}^{n}\right), \left(u_{g,r}^{n+1} - u_{g,r}^{n}\right)\right]$, at all grid points is less than $\epsilon = 1 \times 10^{-6}$. The density is then updated with the new pressure and temperature through the ideal gas law. Using the O2 concentration and temperatures at the new time step, temperature dependent material properties, chemical reaction rate, and extent of reaction are updated and passed to the next simulation loop. Implementation of the above is performed with an in-house Fortran 90 code. A schematic illustrating the full solution procedure is shown in **Figure 2**.

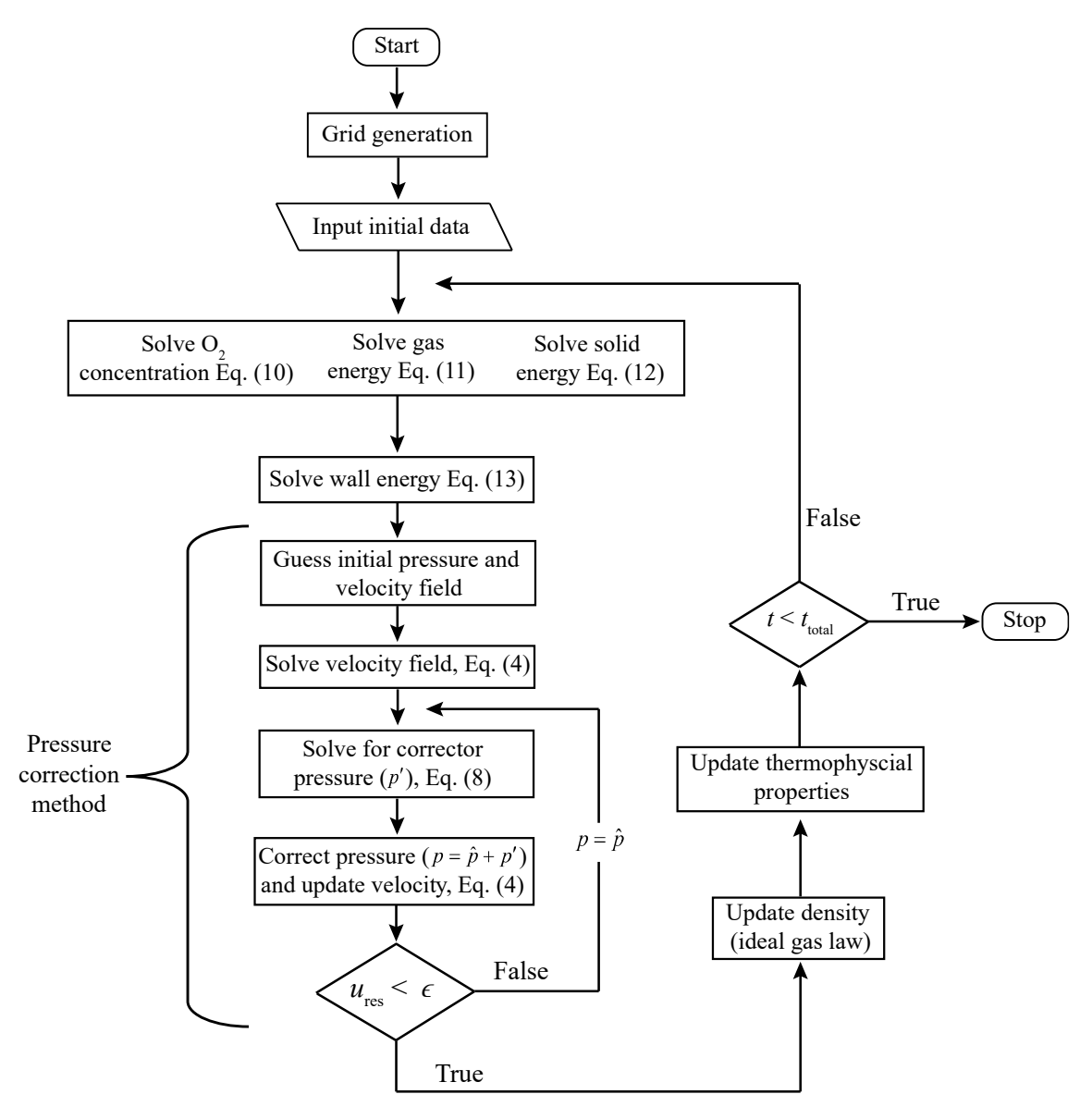


Figure 2: Implementation process for solving the full set of governing equations.

III. Numerical Validation and Results

Two representative experimental cases are used to validate the numerical model: (a) a stationary packed-bed reactor for Fe/Mn binary metal oxides by Wokon et al. [24,26] for both reduction and oxidation steps, and (b) our in-house experimental data for the described moving-bed reactor for reduction. A mesh and time step convergence study is also carried out for the in-house reactor model (**Figure 1**) using the operating conditions described in Sect. III-B. A mesh size of 320×32 (axial × radial nodes) and time step of $\Delta t = 0.0002$ s is found to be sufficient to

capture the sharp thermal gradients and temporal changes in the reactor and is thus used for all simulations. The wall temperature at the quenching zone thermocouple (T_1) , reaction zone thermocouple (T_2) , and the exit oxygen concentration at t = 180 min from the mesh convergence study with $\Delta t = 0.0002$ s are listed in **Table 1**.

As mentioned in the previous section, all validation and simulation results are for the axisymmetric version of the present model, and it is denoted as "2D model" in the rest of this paper. To demonstrate the improvement of the 2D model, the results are compared with those obtained from the 1D model with the Ergun's equation-based plug flow formulation as detailed in [40].

Table 1: Selected results of mesh convergence study

Grid size (axial × radial nodes)	80 × 8	160 × 16	320 × 32	320 × 64	640 × 64	640 × 128
<i>T</i> ₁ (°C)	1492.92	1419.42	1400.77	1401.18	1400.91	1401.04
<i>T</i> ₂ (°C)	55.80	48.09	48.81	48.79	47.18	47.17
O ₂ at exit (%)	4.80	4.57	4.48	4.48	4.42	4.43

A. Validation with Packed Bed Reactor

An experimental study for TCES in a stationary ($u_s = 0$) packed-bed reactor of binary manganese-iron oxides was presented by Wokon et al. [26]. The chemical reaction considered follows

$$6(Mn_{0.75}Fe_{0.25})_2O_3 + \Delta H \Box \quad 4(Mn_{0.75}Fe_{0.25})_3O_4 + O_2.$$
 (19)

Further details for the reaction kinetics can be found in [25]. **Table 2** presents reactor dimensions and key material property and operating parameters used in the experiment (corresponding to Cycle 11 in [25]). The cycle includes both charge (reduction) and discharge (oxidation) steps. First, the inlet gas flow and reactor wall is heated from 940°C to 1040°C within 20 min using a constant air flow rate of 10 NL/min. The temperatures are then held constant for 130 min, after which they are reduced from 1040°C to 400°C at a rate of 5°C/min.

Table 2: Input parameters for reactive packed bed simulation

	17. 1
Parameter	Value
Tube inner diameter	54.3 mm
Tube thickness	2.9 mm
Tube height	195 mm
Thermocouples T_1 , T_2 , T_3 , T_4 (measured from $z = 0$)	10, 50, 90, 130 mm
Particle diameter, d_p	2.42 mm
Bulk density, ρ_{bulk}	1353 kg/m^3
Solid density, ρ_s	5125 kg/m^3
Bulk porosity, ε_b	0.34
Intra-particle porosity, $\varepsilon_{\rm por}$	0.6
Reaction enthalpy, ΔH	271 kJ/kg
\dot{V}_g (volume flow rate)	10 NL/min
Inlet mass fraction of oxygen, $C_{O_2,in}$	23.27%
Outlet gas pressure, $p_{g,\text{out}}$	1.01325 bar
Initial ramp rate for 0 to 20 min (940°C to 1040°C)	+5°C/min
Constant temperature from 20 to 150 min	1040°C
Final cooling rate from 150 min to end (1040°C to 400°C)	-5°C/min

The temperature-dependent parameters used in the simulation can be found in [24]. Throughout the experiment, as the hot gas flowed through the reactor, a portion of thermal energy was lost to the ambient air through natural convection. In order to maintain the needed temperature for the reaction to occur, a heater was added to the outer tube wall, however the magnitude of this additional thermal load was not given in [26]. In order to account for the added thermal load, a parametric study of the solid-wall heat transfer coefficient h_{sw} is conducted to calibrate the model. A value of $h_{sw} = 30 \text{ W/m}^2/\text{K}$ is found to be reasonable and is used for all results shown throughout this section. Transient temperature profiles for the four thermocouples from both the 1D and 2D models are presented in **Figure 3**. Overall, the transient temperature profiles from both models demonstrate reasonable comparison with experimental results. Some discrepancy and time delays are observed (similar time delays were also reported in [24]) and can be attributed to the exact heat input and distribution not being known definitively.

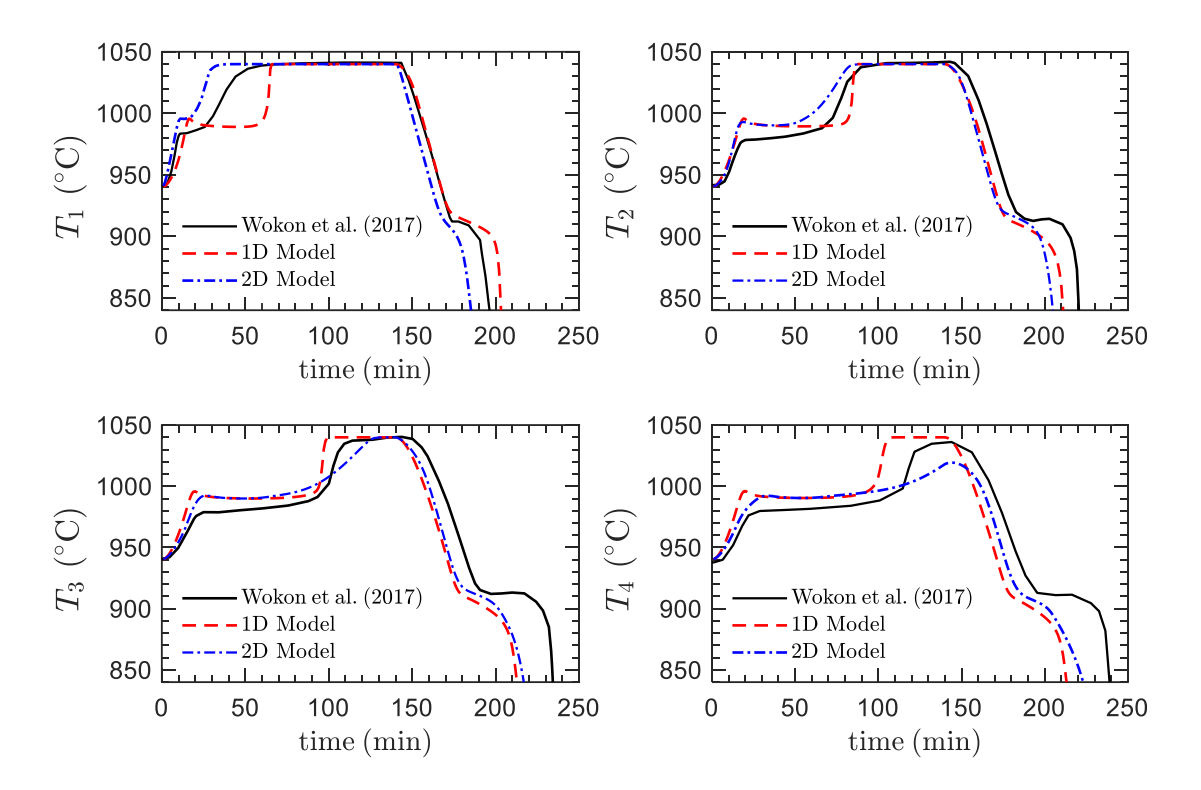


Figure 3: Simulated temperature profiles vs. experimental results for a reactive packed bed reactor.

The predicted overall extent of reaction of the packed bed and oxygen concentration at the reactor outlet were also compared to experimental data in **Figure 4** for both models. It is noted here that the extent of reaction in **Figure 4** is plotted as $1 - \alpha$ to stay consistent with [24]; i.e., the particles are fully reduced at $\alpha = 0$ and fully oxidized at $\alpha = 1$. Overall, the transient trends in the data have reasonable matching. Discrepancies are likely due to a myriad of factors, such as the exact energy input not being known and the time delay previously mentioned. Overall, it can be noticed that the exit oxygen concentration in the 2D model is slightly lower than the 1D model. This could be attributed to the assumption in the 1D model that radial variation is neglected, thus allowing for heat input/lost on the reactor boundaries to dissipate into/out of the domain faster than the 2D model.

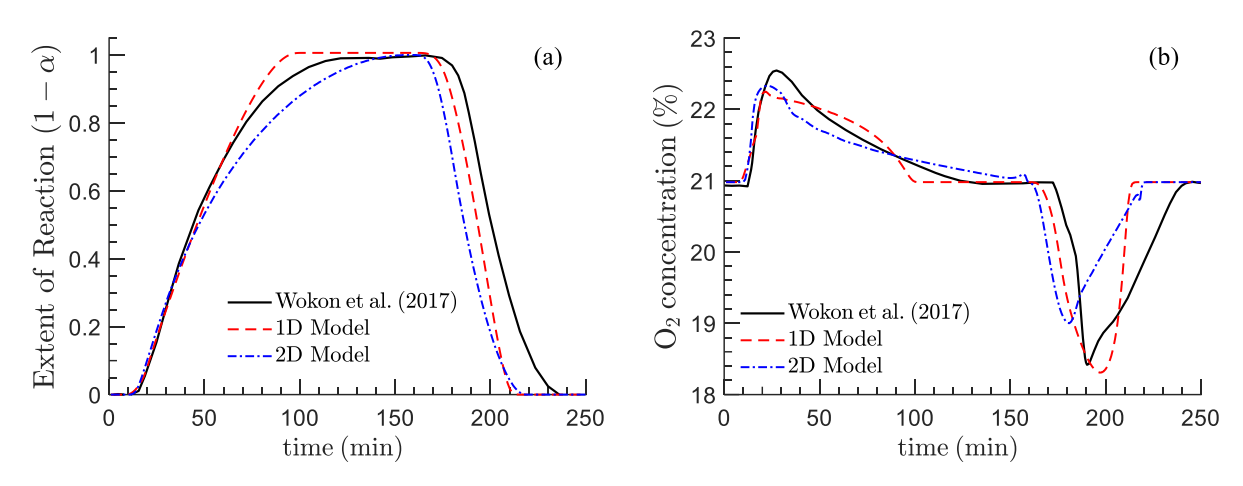


Figure 4: Comparison between numerical model and experimental results for (a) the extent of reaction in the packed bed, and (b) oxygen concentration at the exit.

B. Validation with Moving-bed Reactor

This section describes the validation with the experiments reported in [39] for the reduction reaction. The setup contains a 1420 mm alumina tube with a wrap-around furnace installed (approximately 300 mm in length) at the middle of the tube (see **Figure 1**). The measured temperatures T_1 , T_2 , and T_3 are used for model validation. Both the experiment and simulation begin at room temperature. Initially, fully oxidized particles are placed in the tube and electrical power is supplied to the furnace for 3 hours until T_3 reached 1000°C. A small nitrogen flow of 1 standard liter per minute (SLPM) is supplied during this initial heating phase to avoid air-ingress.

Following the heat-up procedure, the nitrogen and particle flows are initiated at an average rate of 48 SLPM and 0.75 g/s, respectively. The furnace power is then controlled to elicit a linear increase in the control temperature, T_2 , from 1000°C to 1450°C over the span of ~102 min, afterwards it is kept constant at 1450°C. At 87 min, the flow rates of gas and particles are step-changed to 60 SLPM and 1.25 g/s, respectively. These values are chosen to balance the sensible heat across the system ($m_s c_{p,s} = m_g c_{p,g}$). It should also be noted that the gas flow was supplied as a pulsing wave at a low frequency to minimize fluidization in the tube, with the average flow rate of gas in one pulse cycle being used to balance the sensible heat. The pulsations were not included in the numerical model, and instead the average flow rates were used. Remaining information on the reactor geometry, material properties, and operational parameters can be found in **Table 3**.

While the electric power into the furnace, P_{electric} , was recorded during experiments, the details of the power entering the reactor tube were not measured directly. Therefore, to apply the

furnace heating in the 300 mm heated section within the model, two different boundary conditions were implemented in both the 1D and 2D models: (a) a temperature BC in which a uniform tube wall temperature, T_w , is prescribed according to the ramp rate and dwelling temperature mentioned, and (b) a heat flux BC with uniform $q_w = \lambda P_{\text{electric}}/A_w$ imposed, where λ represents the portion of P_{electric} that enters the 300 mm heated zone and A_w is the surface area of the tube in direct contact with the furnace. λ is approximated via a steady state heat loss calibration, i.e., the analysis assumes that the thermal mass of the peripheral furnace components is negligible compared to the mass of reactive material pellets in the tube. Steady state heat loss calibration is performed by maintaining the furnace at different temperatures between 1000 and 1450°C for a long period until input power measurements are steady. The difference in temperature between the furnace and ambient (ΔT_{f-a}) is then plotted against the power at steady state and the slope and vertical intercept of the line (c_f and m_{f-a}) are extracted via linear regression. λ is then estimated using

$$\lambda = 1 - \frac{m_{f-a}\Delta T_{f-a} + c_{f-a}}{P_{\text{electric}}}.$$
 (20)

A final value of $\lambda = 47.5\%$ is found to match the calibrated heat loss and setpoint temperature well and is used throughout. Polynomial fits were used for the electric power as

$$P_{\text{electric}} = \begin{cases} -1.239 \times 10^{-5} t^4 + 4.894 \times 10^{-3} t^3 - 0.4961 t^2 + 39.34 t + 701.1, & \text{for } t < 100 \text{ min} \\ -4.583 \times 10^{-7} t^5 + 3.813 \times 10^{-4} t^4 - 0.1259 t^3 + \\ 20.65 t^2 - 1690 t + 5.799 \times 10^4 & \text{for } t \ge 100 \text{ min} \end{cases}$$
(21)

where t is in minutes and P_{electric} in Watts. A comparison of the measured power and the polynomial fits in Eq. (2) is shown in **Figure 5**.

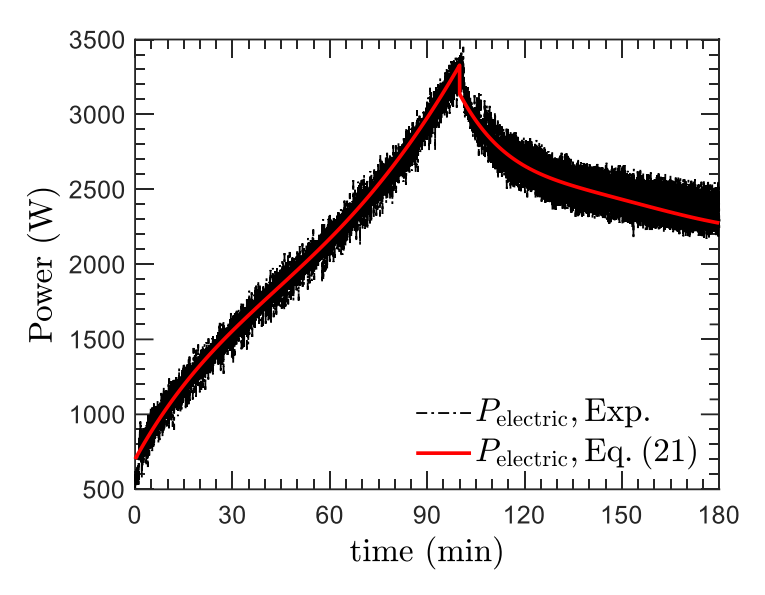


Figure 5: Electrical power input to the furnace.

The chemical reaction of interest is thermal reduction of a magnesium-manganese oxide with nitrogen as purging gas:

$$Mg_xMnO_{1+x+y_1} + \Delta H \square Mg_xMnO_{1+x+y_2} + \frac{y_1 - y_2}{2}O_2.$$
 (22)

Further information on the redox kinetics can be found in [48,57]. It is noted that the reaction rate includes dependencies on both local solid temperature and O₂ partial pressure, thus both are taken into account within the model. It is also pointed out that particles are reduced as they move downward through the tube. Hence, the local extent of reaction must consider a transformation from Lagrangian to Eulerian coordinates within each time step as detailed in [40].

Table 3: Experimental setup of the moving-bed reactor

Parameter	Value		
Tube inner diameter, D_i	50.8 mm		
Tube outer diameter, D_o	57.15 mm		
Tube height	1420 mm		
Thermocouples T_1 , T_2 , T_3 (measured from z = 0)	203, 660, 964 mm		
Particle diameter, d_p	3 mm		
Bulk density, ρ_{bulk}	2003 kg/m^3		
Reaction enthalpy, ΔH	380 kJ/mol		
Bulk porosity, ε_b	0.34		
Alumina tube density, ρ_w	3890 kg/m^3		
Volumetric flow rate of gas, $\dot{V_g}$	48 SLPM for $t < 87 \text{ min}$ 60 SLPM for $t \ge 87 \text{ min}$		

Mass flow rate of solid particles, \dot{m}_s	0.75 g/s for t < 87 min 1.25 g/s for t \geq 87 min			
Inlet gas pressure, $p_{g,in}$	1.084 bar for $t < 87$ min 1.123 bar for $t \ge 87$ min			
Initial ramp rate for 0 to 102 min	4.4°C/min			
Constant temperature for 102 to 180 min	1450°C			

First, solid phase temperatures for selected times are plotted in **Figure 6** and **Figure 7** for the T_w BC and q_w BC, respectively. It is found that the q_w BC produces a narrower high-temperature band in the axial direction of the reactor, while both BC's have similar amounts of radial temperature variation. The difference in the heated zone profiles is due to the total power input from both models, where the q_w BC inputs ~15% less overall power than the T_w BC. This will be demonstrated in more detail in Sect. III-C with a detailed power map for both models.

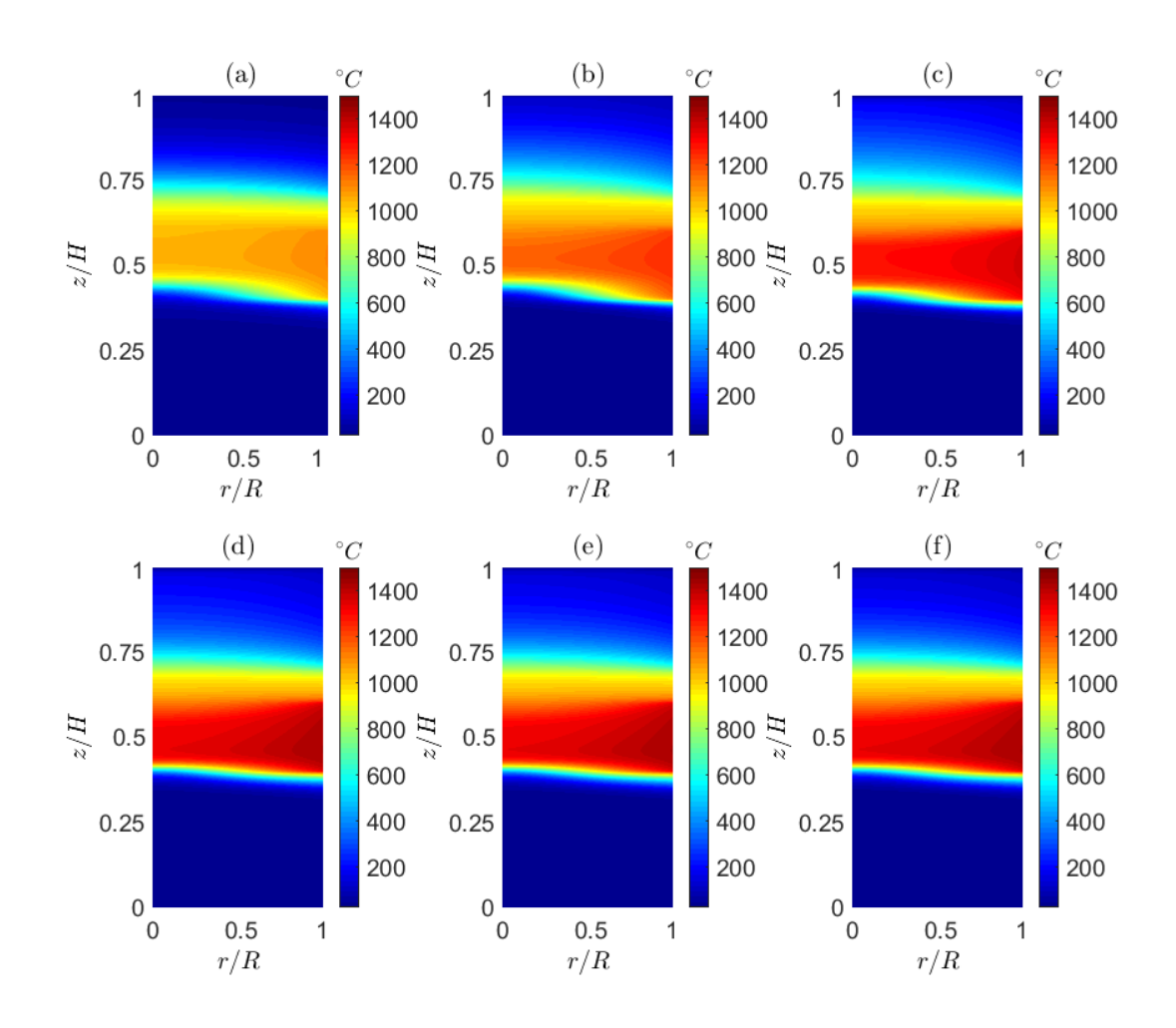


Figure 6: 2D temperature contours for the solid phase within reactor with applied temperature boundary condition at (a) 30 min, (b) 60 min, (c) 90 min, (d) 120 min, (e) 150 min, and (f) 180 min.

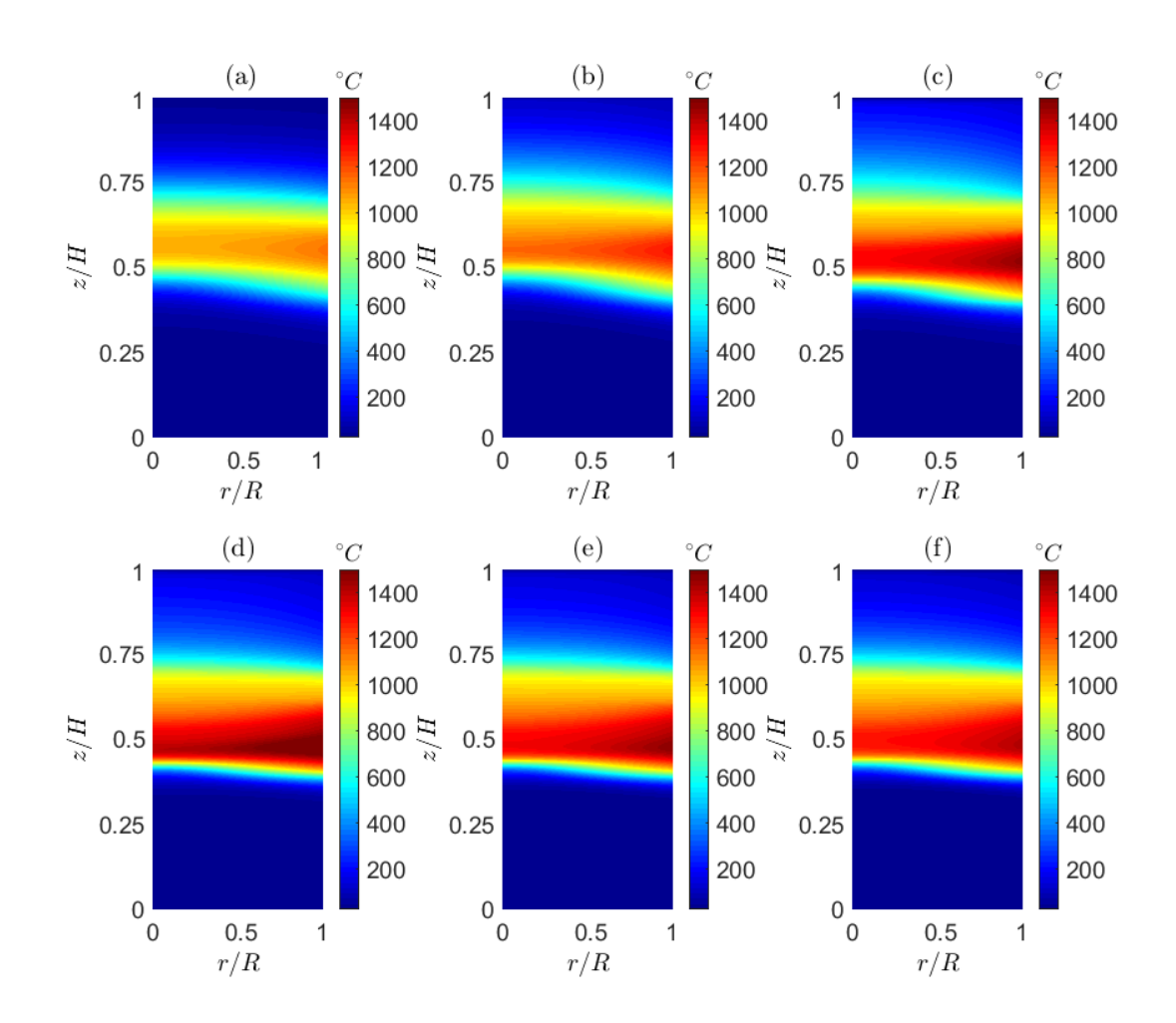


Figure 7: 2D temperature contours for the solid phase within reactor with applied flux boundary condition at (a) 30 min, (b) 60 min, (c) 90 min, (d) 120 min, (e) 150 min, and (f) 180 min.

Figure 8 shows the velocity magnitude and streamlines for the gas phase at discrete times. At all times, the data shows that the flow is largely unidirectional ($u_{g,z} >> u_{g,r}$). Superficial gas velocities in the z-direction are as large as ~2.5 m/s, while velocities in the r-direction only range up to ~0.02 m/s. During the first ~100 minutes, the gas velocity in the reaction zone continues to increase from ~1.3 m/s to ~2.5 m/s as the temperature increases, and then stabilizes thereafter.

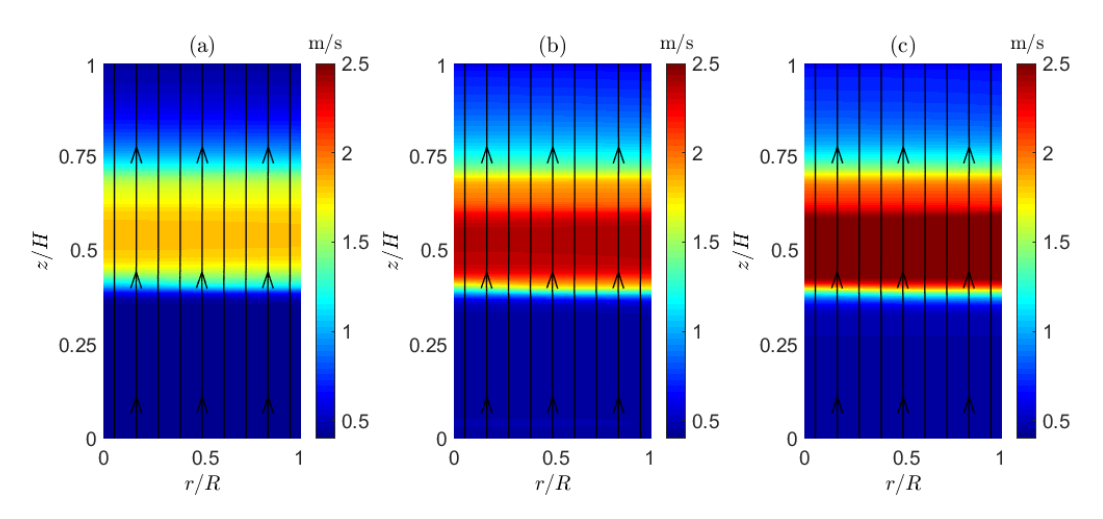


Figure 8: Superficial gas velocity profiles with applied temperature boundary condition at (a) 45 min, (b) 90 min, and (c) 135 min.

Figure 9 and Figure 10 show the radial temperature profiles of the solid phase at z/H = 0.5 for both BCs. The data shows that maximum temperature differences of ~250°C are found between the centerline and tube wall during the first ~90 min with the q_w BC, while this difference reduces to between 50°C and 100°C after this time for both BCs. According to Figure 9, the temperatures in the heated zone are constant after 90 min for the T_w BC. In contrast, Figure 10 shows that the temperatures peak near ~120 min for the q_w BC and continually decrease for the remainder of the simulation. This behavior is accounted to the use of a constant λ . Due to the experimental complexities in obtaining a transient calibration of the furnace heat loss, the constant λ is assumed to match steady state values. Further effects of this assumption on the thermal and concentration fields will be discussed below.

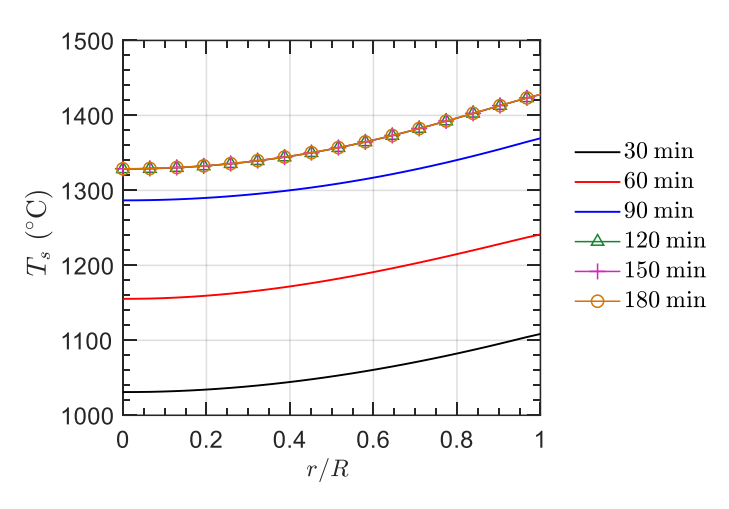


Figure 9: Radial temperature profiles at z/H=0.5 for prescribed temperature boundary condition.

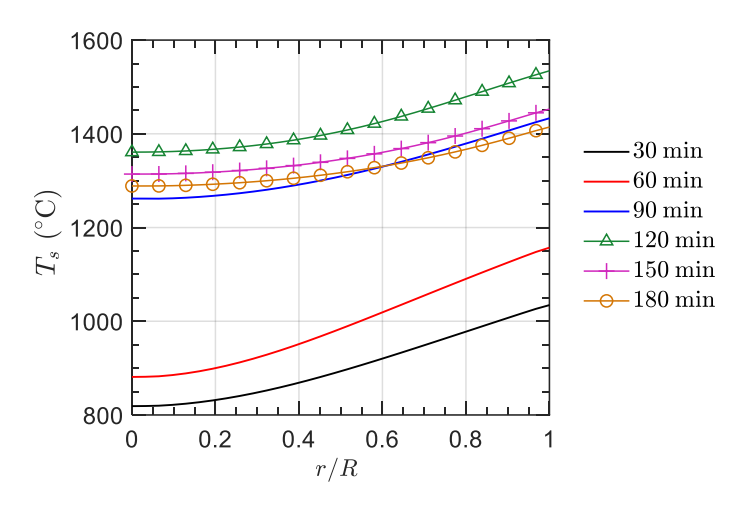


Figure 10: Radial temperature profiles at z/H=0.5 for prescribed flux boundary condition.

To further demonstrate the effectiveness of the three-zone reactor design (see **Figure 1**), we highlight the radial gas and solid temperature profiles at representative axial locations within each of the three zones at t = 180 min in **Figure 11** when using the T_w BC. In addition to the significant radial temperature variations, it is clear that (1) $T_g < T_s$ in the quenching zone, (2) $T_g \sim T_s$ in the reaction zone, and (3) $T_g > T_s$ in the recuperation zone, thus confirming their functions in each zone.

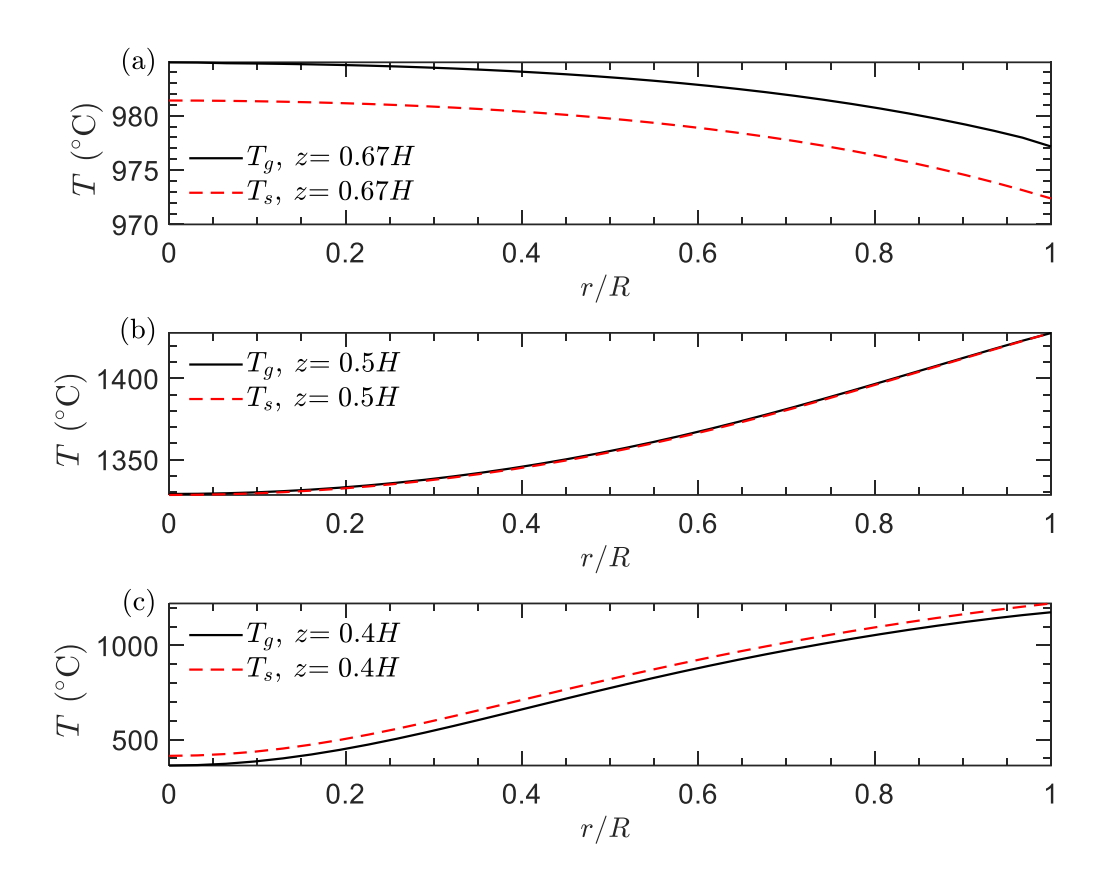


Figure 11: Radial temperature profiles at t = 180 min for gas and solid phases located at (a) z/H = 0.67 in the recuperation zone, (b) z/H = 0.5 in the reaction zone, and (c) z/H = 0.4 in the quenching zone.

Next, the distributions of O_2 concentration and reaction extent in the reactor are shown in **Figure 12** and **Figure 13** for the q_w BC at select times. It should be noted that the extent of reduction in **Figure 13** is denoted by $1 - \alpha$ according to the definition in Eq. (3). In comparison to the temperature field in **Figure 9** and **Figure 10**, it is obvious that the radial deviations are more significant for the distribution of O_2 concentration and extent of reaction. For sensible heat storage, the implications of radial temperature deviation are typically not severe, as thermal equilibrium within a bed will still be reached after longer heat-up times. However, the reaction kinetics involved with TCES are largely governed by local particle temperature. For this reason, while the differences shown in **Figure 6-Figure 10** appear miniscule, their effects on reaction rate are significant as evidenced in **Figure 12** and **Figure 13**.

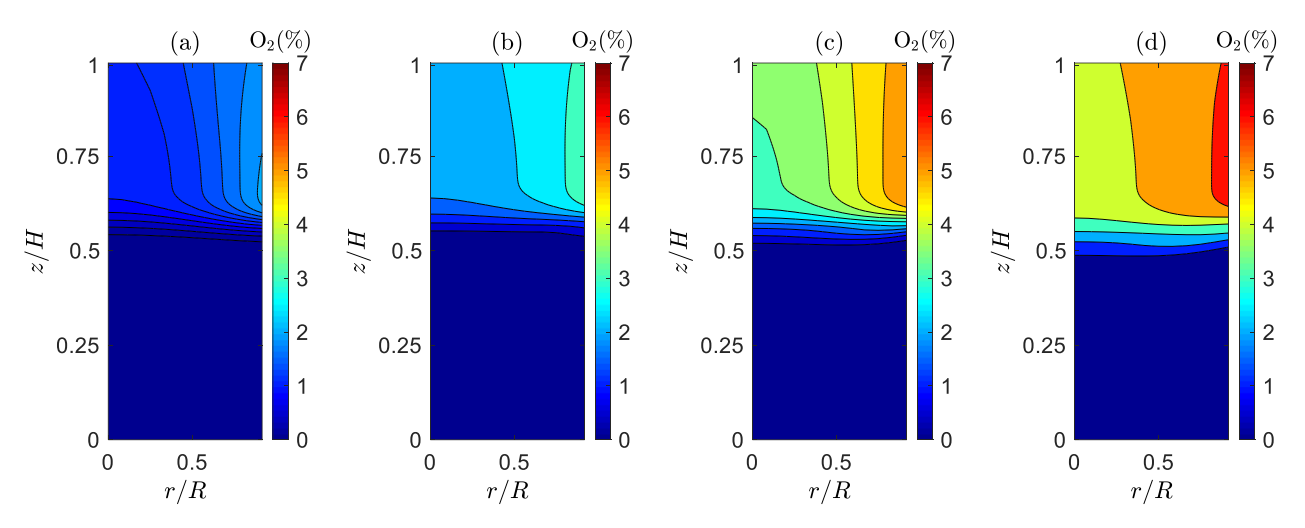


Figure 12: Radial-axial oxygen concentration contours within reactor with applied flux boundary condition at (a) 30 min, (b) 60 min, (c) 90 min, (d) 120 min.

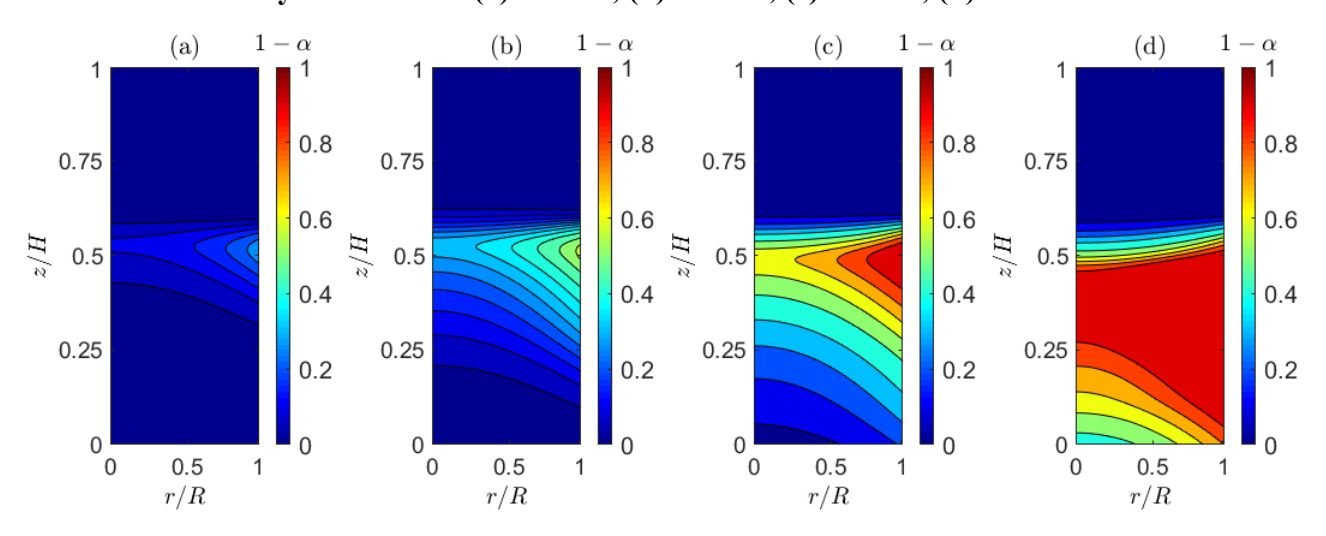


Figure 13: Radial-axial reaction extent within reactor with applied flux boundary condition at (a) 30 min, (b) 60 min, (c) 90 min, (d) 120 min.

Furthermore, the axial profiles of the tube wall temperature are plotted in **Figure 14**. We make two main observations from **Figure 14** and the preceding discussion. First, in comparing **Figure 14a** and **Figure 14b**, the implications of the T_w BC and q_w BC are apparent; where the T_w BC commands a flat temperature profile in the heated zone, while the power input BC creates a smoother peaking trend. Second, better temperature matching with experiments is observed for the 2D models and the differences between 1D and 2D is more pronounced in regions with large temperature gradients.

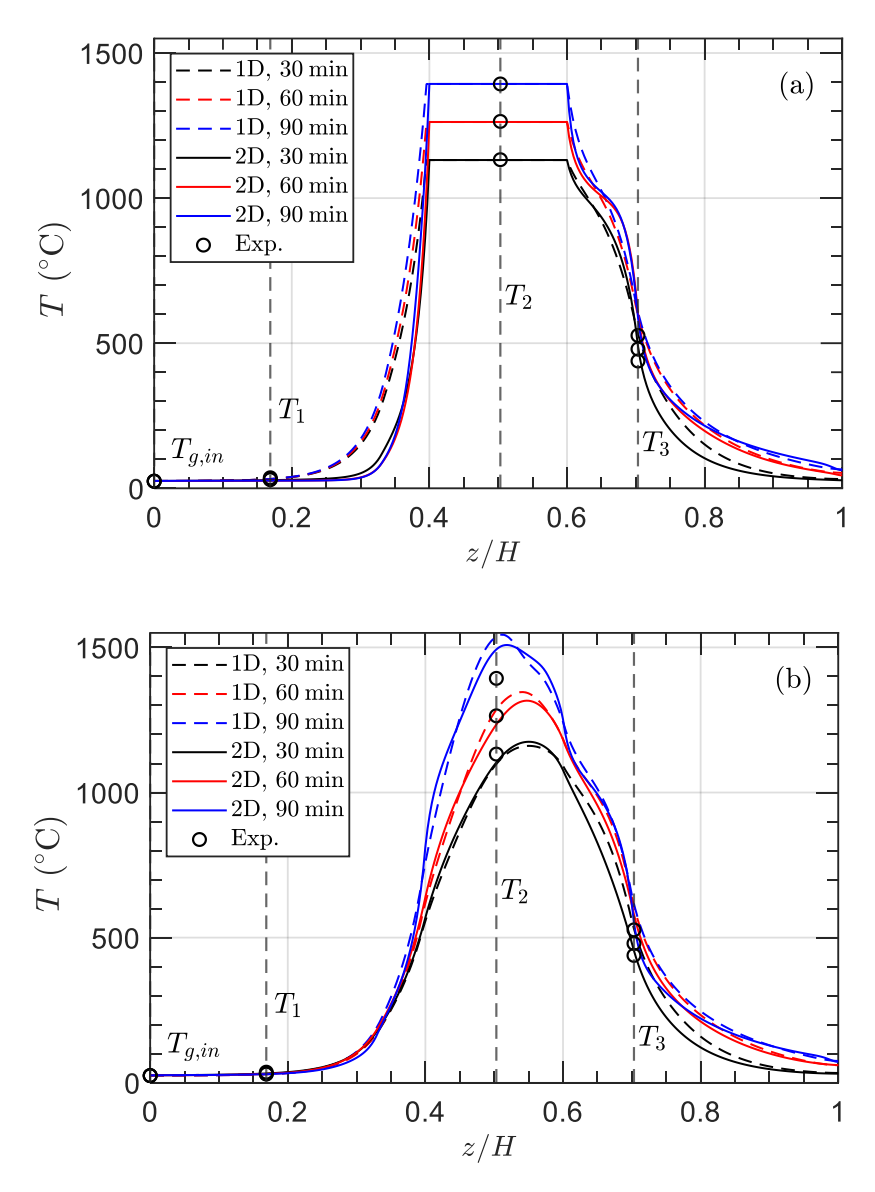
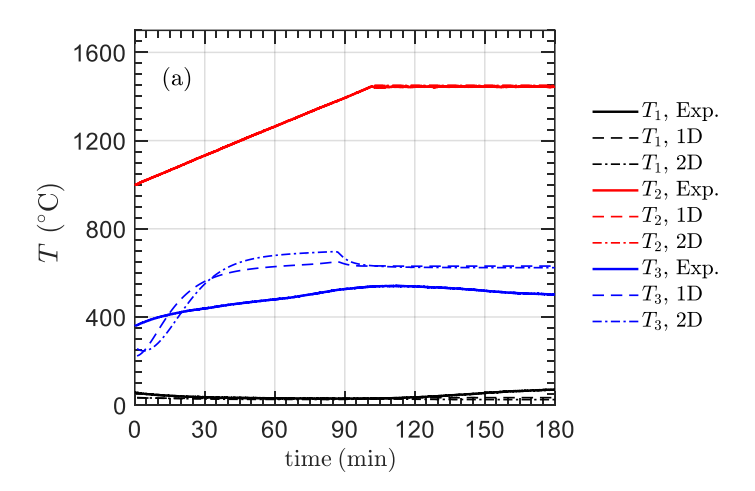


Figure 14: Axial varying wall temperatures for selected thermocouples for (a) prescribed temperature boundary condition and (b) prescribed flux boundary condition.

Transient temperature profiles and exiting O_2 concentration are illustrated in **Figure 15** and **Figure 16**, respectively. For comparison, experimentally measured values are included in the figures. The large oscillations in experimental data observed in **Figure 16** are consequence of the pulsating gas flow previously mentioned. The maximum deviation seen with the T_w BC is at thermocouple T_3 , with steady state differences of approximately 200°C. In comparison, the prescribed flux BC shows deviations with T_2 and T_3 in the range of ~100-150°C. Slight improvement is discerned with the 2D model. In **Figure 16**, it is shown that the O_2 concentration predicted with both BCs are lower for the 2D model. For the first 100 min, both BCs predict similar

trends in O_2 , however the T_w BC predicts a constant O_2 for the remainder of the time while a steady decrease is noted with the q_w BC. This steady decrease is attributed to the assumption of a constant λ as previously discussed. Overall, each model and BC presents reasonable agreement, with some improvements in the 2D model.

The observed temperature and O_2 differences are attributed to three sources: (1) heat transfer coefficient correlations, (2) properties of insulating material, and (3) assumptions associated with heated zone boundary conditions. For (1), it is noted that most correlations available in literature were not constructed at the high temperatures studied here, and thus further extension of those works would be necessary for model improvement. In the experimental setup, insulation layers were packed and secured around the tubular walls (see **Figure 1**). During this process, it is likely that the insulation will be compressed to some degree, thus modifying the thermal conductivity from standard catalog values used in the model. Nonetheless, with the likely discrepancies in heat transfer coefficients and insulation properties and the unknowns associated with the T_w BC and q_w BC (constant λ), the predicted temperatures and O_2 agree very well with experimental results; thus the model is considered validated.



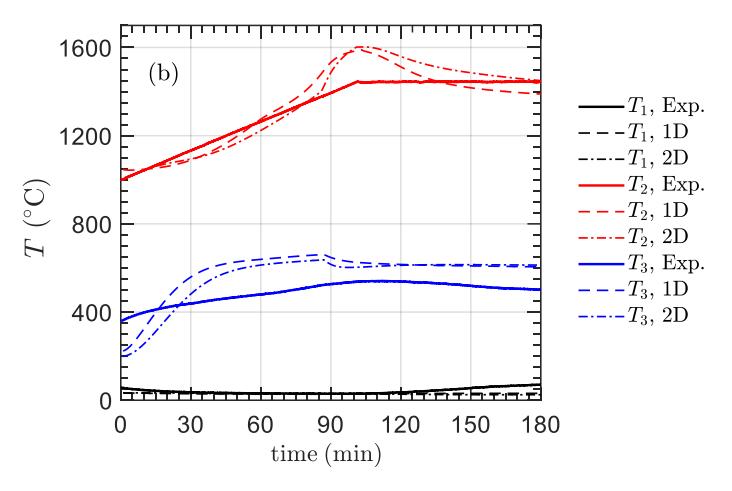


Figure 15: Temperature comparisons at thermocouple locations $(T_1, T_2, \text{ and } T_3)$ for (a) prescribed temperature boundary condition and (b) prescribed flux boundary condition.

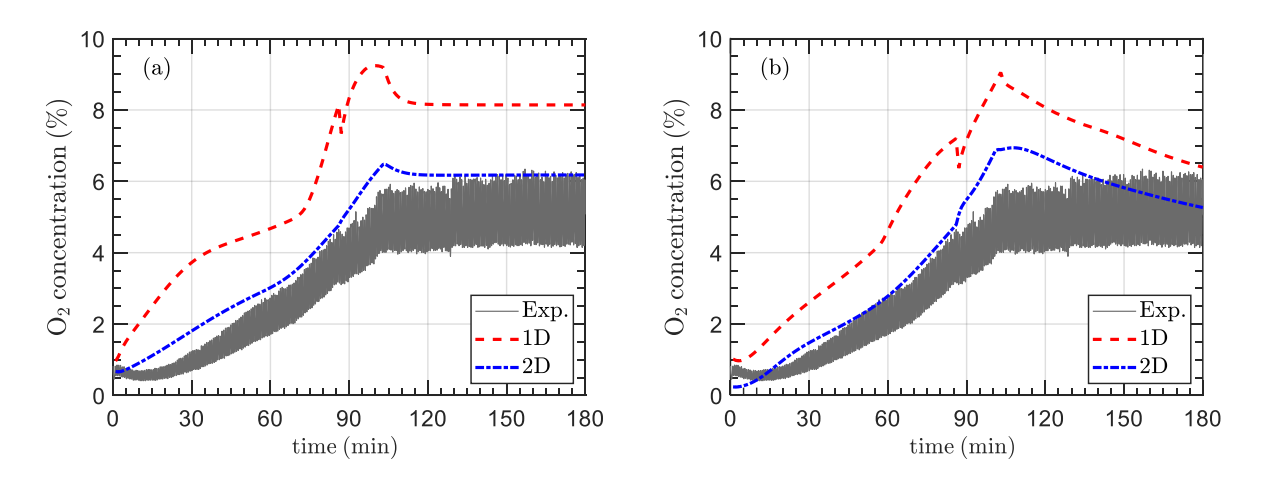


Figure 16: O₂ concentration at outlet of reactor simulated for (a) prescribed temperature boundary condition and (b) prescribed flux boundary condition.

C. Energy Map and Efficiency Analysis

In this section, we consider three efficiencies to describe the effectiveness of the reactor following [39]: (1) electrical-to-chemical efficiency, denoted as η_{turnace} , (2) thermal input-to-chemical (thermochemical) efficiency, denoted as η_{tc} , and (3) total energy input-to-chemical efficiency, denoted as η_{system} . The corresponding definitions are

$$\eta_{\text{furnace}} = \frac{\int\limits_{A_{\text{cs}}} \alpha_{\text{out}} u_{s,\text{out}} (\rho_{\text{ox}} - \rho_{\text{red}}) \Delta H dA_{\text{cs}} + \int\limits_{V_{\text{bed}}} \frac{d\alpha}{dt} (\rho_{\text{ox}} - \rho_{\text{red}}) \Delta H dV}{P_{\text{electric}}},$$
(23)

$$\eta_{\text{tc}} = \frac{\int_{A_{\text{cs}}} \alpha_{\text{out}} u_{s,\text{out}} \left(\rho_{\text{ox}} - \rho_{\text{red}} \right) \Delta H dA_{\text{cs}} + \int_{V_{\text{bed}}} \frac{d\alpha}{dt} \left(\rho_{\text{ox}} - \rho_{\text{red}} \right) \Delta H dV}{P_{\text{electric}} - \dot{Q}_{\text{loss}}},$$
(24)

and

$$\eta_{\text{system}} = \frac{\int_{A_{\text{cs}}} \alpha_{\text{out}} u_{s,\text{out}} (\rho_{\text{ox}} - \rho_{\text{red}}) \Delta H dA_{\text{cs}} + \int_{V_{\text{bed}}} \frac{d\alpha}{dt} (\rho_{\text{ox}} - \rho_{\text{red}}) \Delta H dV}{P_{\text{electric}} + \dot{Q}_{O,\text{sep}} + P_{\text{pump}}}$$
(25)

where \dot{Q}_{loss} is the rate of thermal energy lost on the outside of the tube due to natural convection and radiation, $\dot{Q}_{0_2,sep}$ is the power required to separate oxygen from nitrogen, and P_{pump} is the power required for the gas to be moved through the bed. The first term in the numerator of Eqs. (22-24) is the rate of chemical potential energy leaving the tube through the particles. Since radial variation is considered in the model, integration over the area in which particles exit, A_{cs} , is required. The second term refers to the rate of chemical potential energy being generated within the inner volume of the reactor tube, V_{bed} . It is noted that for steady state, the second term will vanish since da/dt will go to zero. Furthermore, the oxygen separation energy can be obtained by [58]

$$\dot{Q}_{O_2, \text{sep}} = -\frac{\dot{\eta}_{N_2} R T_{\text{sep}}}{\eta_{\text{sep}}} \left[\ln(1 - \gamma_{O_2}) + \frac{\gamma_{O_2}}{1 - \gamma_{O_2}} \ln(\gamma_{O_2}) \right]$$
(26)

where $\dot{\eta}_{N_2}$ is the molar flow rate of nitrogen being input into the system, T_{sep} is the operational temperature of the solid oxide separation membrane and taken as 900°C, γ_{O_2} is the mole fraction of oxygen at the outlet, and η_{sep} is the efficiency of the separation and taken as 10% [59]. The pumping energy is obtained from

$$P_{\text{pump}} = \frac{\Delta p_{\text{avg}} \dot{V}_{\text{avg}}}{\eta_{\text{pump}}} \tag{27}$$

where $\Delta p_{\rm avg}$ is the average pressure drop across the bed, $\dot{V}_{\rm avg}$ is the average volumetric flow rate of the gas and $\eta_{\rm pump}$ is the efficiency of the pump and taken here as 50% [60]. The remaining power components are defined as

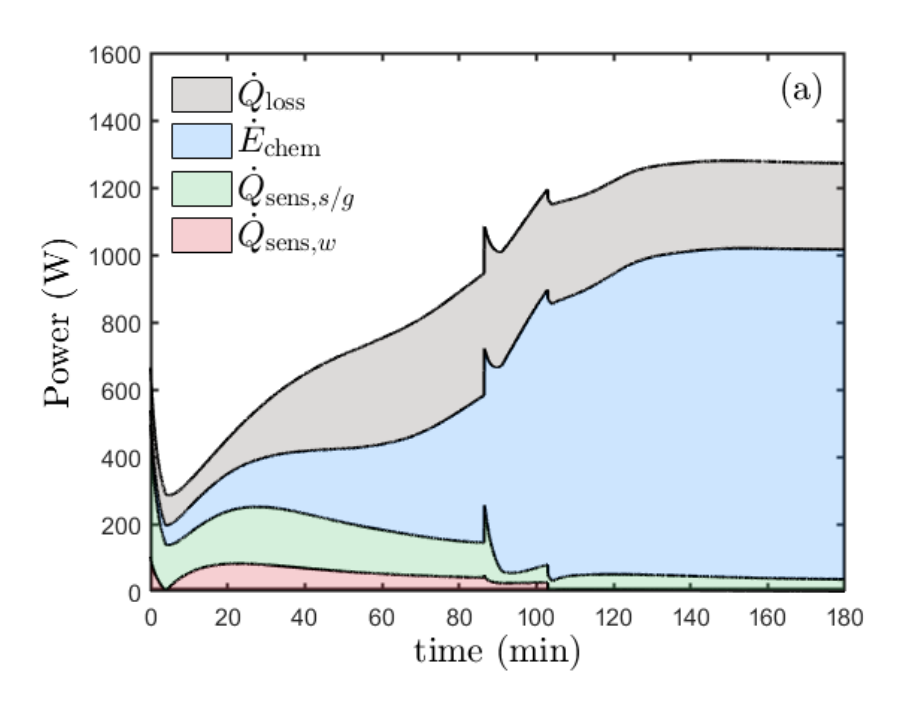
$$\dot{E}_{\text{chem}} = \int_{A_{\text{cs}}} \alpha_{\text{out}} u_{s,\text{out}} (\rho_{\text{ox}} - \rho_{\text{red}}) \Delta H dA_{\text{cs}} + \int_{V_{\text{bod}}} \frac{d\alpha}{dt} (\rho_{\text{ox}} - \rho_{\text{red}}) \Delta H dV, \qquad (28)$$

$$\dot{Q}_{\text{sens},s/g} = \left[\int_{A_{\text{cs}}} \rho_s u_s c_{p,s} T_s dA_{\text{cs}} \right]_{\text{out}} - \left[\int_{A_{\text{cs}}} \rho_s u_s c_{p,s} T_s dA_{\text{cs}} \right]_{\text{in}} + \int_{V_{\text{bed},s}} \rho_s c_{p,s} \frac{\partial T_s}{\partial t} dV + \left[\int_{A_{\text{cs}}} \rho_g u_g c_{p,g} T_g dA_{\text{cs}} \right]_{\text{out}} - \left[\int_{A_{\text{cs}}} \rho_g u_g c_{p,g} T_g dA_{\text{cs}} \right]_{\text{in}} + \int_{V_{\text{bed},g}} \rho_g c_{p,g} \frac{\partial T_g}{\partial t} dV , \tag{29}$$

and

$$\dot{Q}_{\text{sens},w} = \int_{V_w} \rho_w c_{p,w} \frac{\partial T_w}{\partial t} dV, \qquad (30)$$

where $\dot{E}_{\rm chem}$ is the total chemical energy stored during the reduction reaction, $\dot{Q}_{{\rm sens},s/g}$ is the sensible heat absorbed by the gas and solid particles, and $\dot{Q}_{{\rm sens},w}$ is the sensible heat of the reactor tube wall. The power budget for both BCs is depicted in **Figure 17**. The sharp changes observed in **Figure 17** are due to the step change in solid and gas flow rate at 87 min and from the sudden change of the power input from the furnace at ~100 min. It is also noted that since λ is considered constant, q_w continues to decrease at 180 min. The simulation is thus extended to 250 minutes, with q_w being kept constant as evaluated at 180 min in order to reach a steady state condition. During the first ~100 minutes, sensible heat storage in the tube wall and the gas/solid phases plays a significant role, however both become negligible once the initial heating phase is completed. Overall, both models present similar trends, with a slightly reduced power input into the heated zone for the q_w BC.



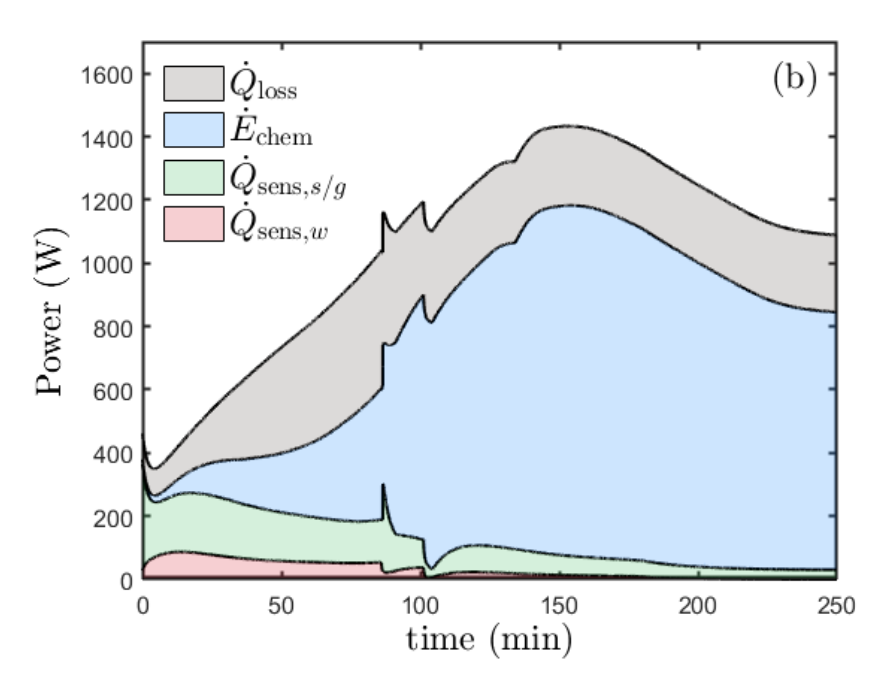


Figure 17: Power budget map for (a) prescribed temperature boundary condition and (b) prescribed flux boundary condition.

Next, the described efficiencies are presented in **Figure 18** for both boundary conditions. Very similar trends are shown in both models, with slightly lower values observed with the prescribed flux BC. The efficiencies were also determined experimentally for steady-state conditions in [39] as $\eta_{\text{furnace}} \sim 40\%$, $\eta_{\text{tc}} \sim 95\%$, and η_{system} between 28%-30%. It is noted that the determination of \dot{E}_{chem} is based on the enthalpy of reaction ΔH and the apparent kinetic model developed based on experiments for Mg-Mn-O cycling between 1000 and 1500°C in our previous work [48]. However, with the prescribed flux BC, the bed temperature may become higher than 1500°C. The assumed extrapolation of the kinetic model for this temperature range may cause slight over/under-prediction of the thermochemical efficiency η_{tc} . Overall, the predicted efficiencies from simulation are in reasonable agreement with these reported values. It is pointed out that the current reactor has not been optimized for maximum efficiency. Parametric studies on key attributes (reactor diameter and length, particle size and bed porosity, furnace temperature, solid/gas flow rates, particle residence time etc.) can be performed with the present model to provide valuable insights into maximizing the reactor system efficiency.

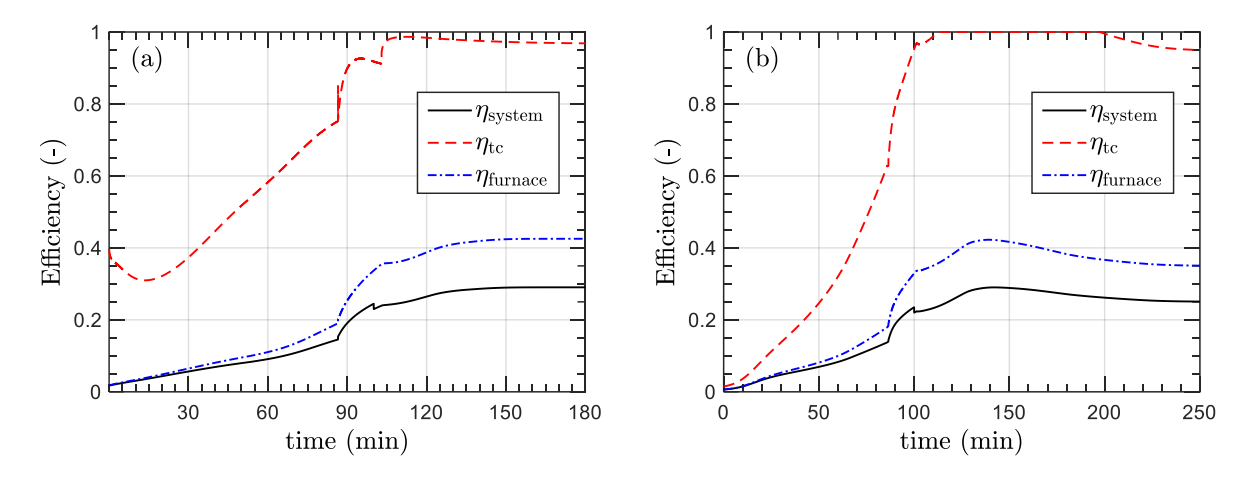


Figure 18: Efficiency comparison for (a) prescribed temperature boundary condition and (b) prescribed flux boundary condition.

D. Influence of Tube Diameter on Reactor Performance

In this section, a study on the effects of the reactor tube diameter is performed to demonstrate the advantages of the 2D axisymmetric model in comparison to its 1D counterpart [40]. Five inner diameters are considered in the study ($D_i = 50$, 62.5, 75, 100, and 125 mm) and a constant wall thickness of 3.175 mm is assumed. In order to stay consistent with the experiment described in Sect. III-B, the mass flow rate of solid particles is scaled for each tube size to maintain the same solid velocity, i.e., the same residence time, and the corresponding inlet gas flow rate is determined from $\dot{m}_s c_{p,s} = \dot{m}_g c_{p,g}$ for heat recuperation. The simulations are performed using the prescribed temperature boundary condition. The solid phase temperatures at t = 180 min for the different reactor tube sizes are given in **Figure 19**. The temperature variation in the r-direction appears minute for the smaller tube diameters (< 75 mm), while for larger diameters (100, 125 mm), the high-temperature zone is largely confined to the near-wall region.

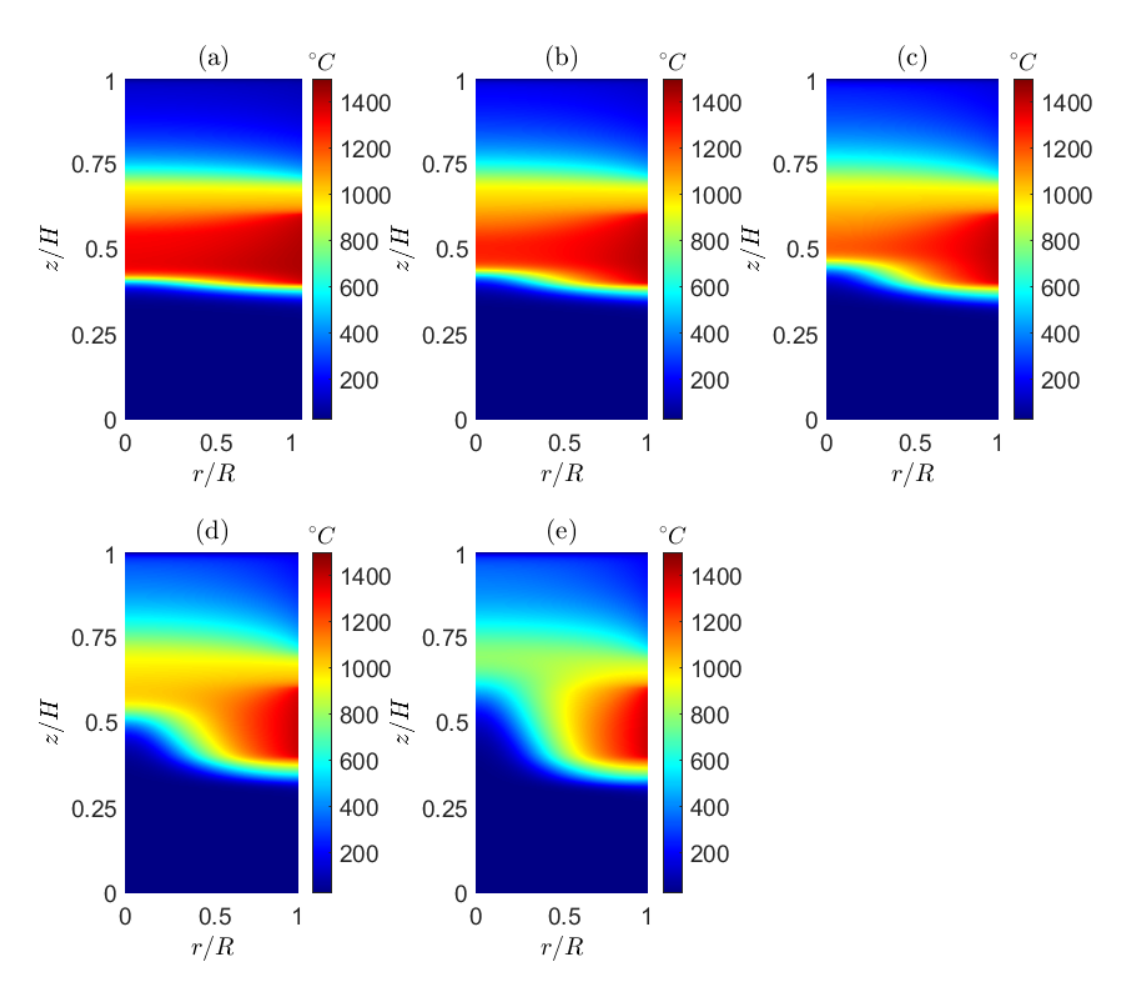


Figure 19: 2D temperature contours for the solid phase within reactor at t = 180 min for inner reactor tube diameters of (a) 50 mm, (b) 62.5 mm, (c) 75 mm, (d) 100 mm, and (e) 125 mm.

This is shown in detail in **Figure 20** with corresponding radial temperature profiles at the mid-height (z/H = 0.5) at t = 180 min. For the smallest tube diameter ($D_i = 50$ mm), the radial temperature difference is near 90°C, while for the largest tube diameter ($D_i = 125$ mm), the temperature difference is near 1200°C. This extreme radial variation has large implications on reactor performance and efficiency, as the particle reduction will be limited near the tube centerline with larger diameters. **Figure 21** shows this variation of reaction extent within the different sized tubes at t = 180 min. As can be seen, the reaction extent near the centerline decreases as the tube size increases, with the largest tube diameter ($D_i = 125$ mm) exhibiting a significant amount of unreacted solid phase at the center of the tube.

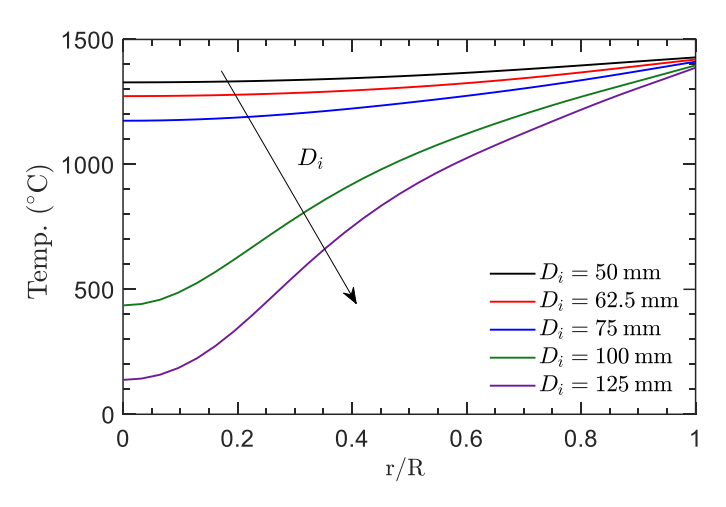


Figure 20: Radial solid phase temperature profiles at t = 180 min and z/H = 0.5 for varied reactor tube diameters

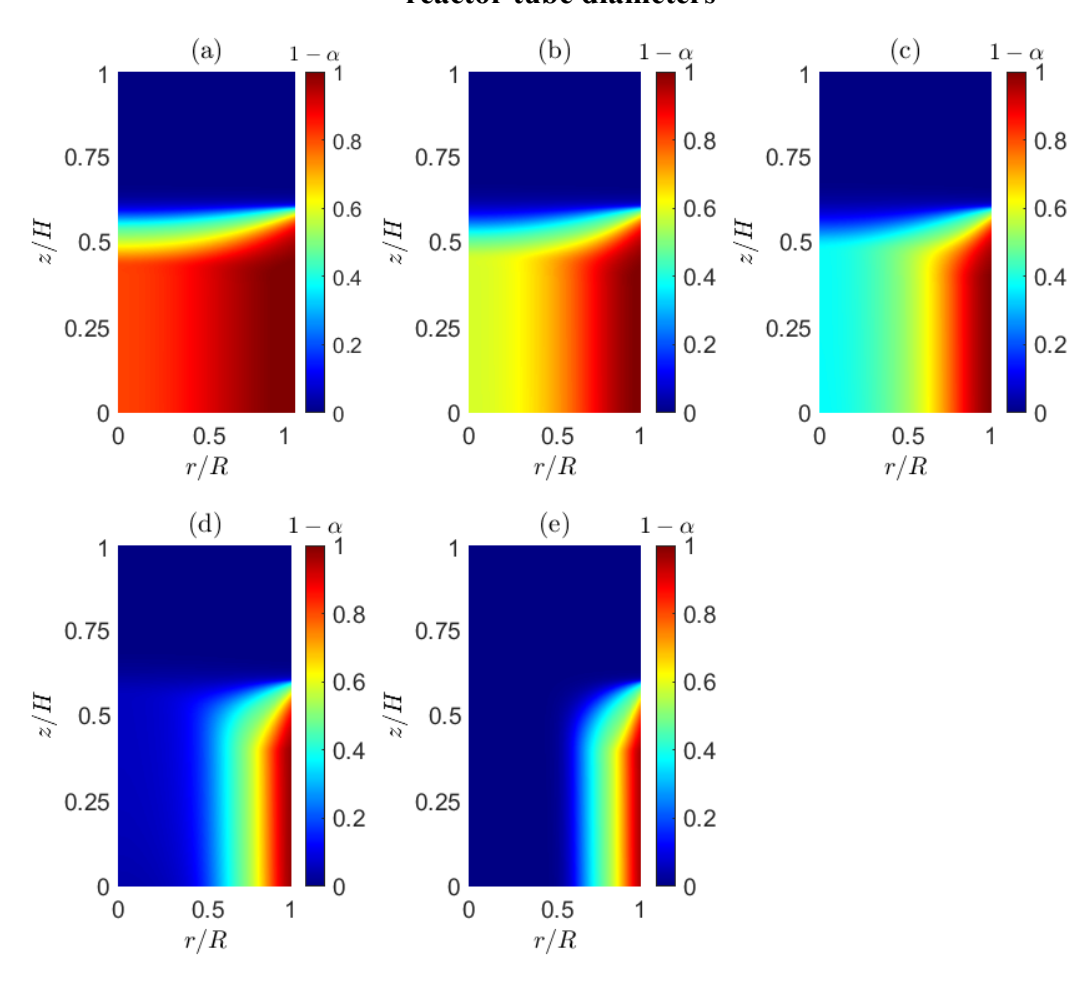


Figure 21: Radial-axial reaction extent within reactor at t = 180 min for inner reactor tube diameters of (a) 50 mm, (b) 62.5 mm, (c) 75 mm, (d) 100 mm, and (e) 125 mm.

Furthermore, a quantitative comparison of reaction extent at the reactor outlet for the different tube diameters is shown in **Figure 22**. The effects of the tube diameter are quite clear, as the particles in the smallest tube reactor ($D_i = 50 \text{ mm}$) are almost completely reduced, while nearly half of the particles in the largest reactor ($D_i = 125 \text{ mm}$) are unreacted. The major assumption of the 1D modeling paradigm is that radial temperature variation is negligible, i.e., $\partial T/\partial r = 0$. While this is a valid assumption for small tube diameters ($D_i \le \sim 50 \text{ mm}$), the results shown here (**Figure 19 – Figure 22**) clearly demonstrate the limitations of a 1D approach and the necessity of considering radial variation in tubular reactor designs.

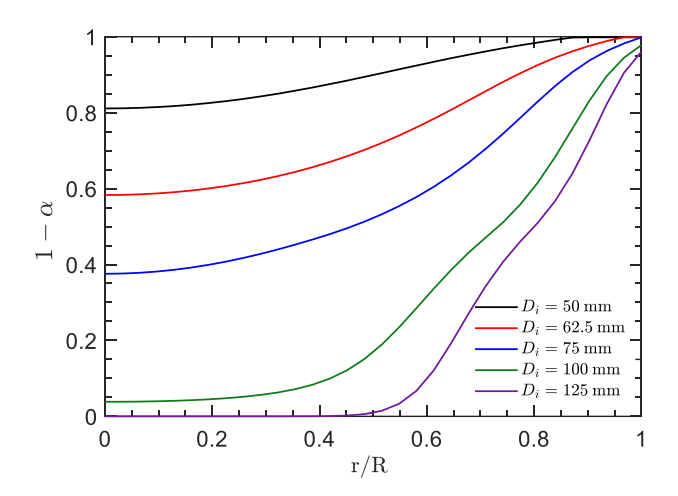


Figure 22: Radial reaction extent profiles at t = 180 min and z/H = 0 for varied reactor tube diameters.

IV. Conclusions

In this paper, a continuum model coupling heat and mass transfer and high-temperature thermochemical reactions for particle-bed reactors is developed and validated. The validation includes comparisons with experimental results for a stationary packed-bed reactor undergoing a redox cycle presented by [26], as well as in-house experiments for the reduction of magnesium-manganese-oxide particles up to 1450°C in a novel moving-bed reactor with inherent heat recuperation [39]. In addition, direct comparison of the 2D axisymmetric version of the present model and its reduced 1D version neglecting radial variations are also conducted, including a comparison of several reactor sizes. The following conclusions can be drawn from this study:

- Comparing the 1D and 2D models, the maximum temperature discrepancy in the radial direction is on the order of ~250°C during heat up phases and reduced to ~100°C during steady operation for the present TCES moving-bed reactor design.
- With the radial effects included in the 2D model, the distributions of O₂ concentration and extent of reaction within the reactor varied drastically in the radial direction. This is attributed to the strong dependence of the reaction kinetics on local solid phase temperatures.
- The two representative boundary conditions within the reaction zone of the moving-bed reactor, with prescribed temperature and heat flux conditions, were able to reasonably match the measured temperatures and O₂ release in experiments. Overall, the heat flux boundary condition case better predicted the temperatures in regions with drastic thermal gradients.
- The reactor tube diameter is found to strongly influence reactor performance. With a given particle-bed residence time, tube diameters near ~50 mm demonstrated close to uniform particle reaction extent and temperature variation in the *r*-direction; however, larger tube sizes (>100 mm) showed decreased reactor performance as the high-temperature zone did not completely penetrate to the centerline of the tube. These effects are uncaptured by a 1D model, clearly demonstrating the advantage of the multi-dimensional model.
- The present coupled model is able to accurately account for the transient and steady power
 components in the system and predict the energy conversion efficiencies of the reactor,
 confirming its applicability and attractiveness in reactor design, scale-up, performance
 prediction, and parameters optimization to provide valuable insights in determining the
 optimal operating procedure and maximizing the system thermochemical energy storage
 efficiency.
- Finally, it is worth noting that while the boundary conditions and the presented simulation results are in 2D, all the governing equations are in vector forms and the numerical methodology can be directly extended to 3D with modified thermal boundary conditions. Hence the present model can also be coupled with external radiation modeling to update the net flux boundary conditions and serve as a valuable tool for TCES modeling with other reactor configurations.

Acknowledgments

This material is based upon work supported by the U.S. Department of Energy's Office of Energy Efficiency and Renewable Energy (EERE) under the Solar Energy Technologies Office (SETO) Award Number DE-EE0008992. L. Li also acknowledges the support from the U.S. National Science Foundation (NSF award number OIA 2031701).

Appendix A: Table of thermophysical properties and correlations (T in K if not specified).

Parameter	Symbol	Value/Correlation	Units	Ref.
Total porosity	ε	$0.375 + 0.34 \frac{d_p}{D_i}$	/	[61]
Gas (N ₂) thermal conductivity	k_g	$ \begin{array}{l} 1.01805 \times 10^{-20} T^6 - 1.71098 \times 10^{-17} T^5 \\ -2.26255 \times 10^{-14} T^4 + 8.53554 \times 10^{-11} T^3 \\ -1.03690 \times 10^{-7} T^2 + 1.14337 \times 10^{-4} T - 1.08670 \times 10^{-3} \end{array} $	W/m/K	
Bulk effective thermal conductivity	$k_{ m bulk,eff}$	$2.5760 \times 10^{-17} T^{6} - 1.0400 \times 10^{-13} T^{5}$ $+1.7301 \times 10^{-10} T^{4} - 1.5273 \times 10^{-7} T^{3}$ $+8.0236 \times 10^{-5} T^{2} - 3.1566 \times 10^{-2} T + 12.9662$	W/m/K	
Solid effective thermal conductivity	$k_{s, m eff}$	$k_{s, ext{eff}} = k_{ ext{bulk,eff}} - arepsilon_b k_g$	W/m/K	[24]
Alumina tube thermal conductivity	$k_{_{\scriptscriptstyle W}}$	$5.5 + 34.5e^{-3.3 \times 10^{-3} (T_w - 273.15)}$	W/m/K	[62]
Gas heat capacity	$c_{p,g}$	$\begin{cases} \frac{1}{M_{N_2}} \left[28.98641 + 1.853978 \left(\frac{T_g}{1000} \right) - 9.647459 \left(\frac{T_g}{1000} \right)^2 \right], \\ +16.63537 \left(\frac{T_g}{1000} \right)^3 + 0.000117 \left(\frac{T_g}{1000} \right)^{-2} \end{cases}, \\ \frac{1}{M_{N_2}} \left[19.50583 + 19.88705 \left(\frac{T_g}{1000} \right) - 8.598535 \left(\frac{T_g}{1000} \right)^2 \right], \\ +1.369784 \left(\frac{T_g}{1000} \right)^3 + 0.527601 \left(\frac{T_g}{1000} \right)^{-2} \end{cases}, \\ 500K \le T_g \le 2000K \end{cases}$	J/kg/K	[63]
Solid heat capacity	$C_{p,s}$	$-2.503 \times 10^{-16} T_s^{-6} + 1.4394 \times 10^{-12} T_s^{-5} - 3.228 \times 10^{-9} T_s^{-4} +3.6473 \times 10^{-6} T_s^{-3} - 2.3635 \times 10^{-3} T_s^{-2} + 1.0435 T_s + 676.24$	J/kg/K	Note: T_s in [°C] here

Alumina tube heat capacity	$C_{p,w}$	$1.04 \times 10^{3} + 1.74 \times 10^{-1} T_{w} - 1.271 \times 10^{-4} T_{w}^{2}$	J/kg/K	[62]
Solid-gas heat transfer coefficient	h_{gs}	$\left(2+1.2\mathrm{Re}^{\frac{1}{2}}\mathrm{Pr}^{\frac{1}{3}}\right)\frac{k_g}{d_p}$	W/m ² /K	[49]
Gas-wall heat transfer coefficient	h_{gw}	$\left(0.023\mathrm{Re}^{\frac{4}{5}}\mathrm{Pr}^{\frac{2}{5}}\right)\frac{k_g}{D_i}$	W/m ² /K	[51]
Solid-wall heat transfer coefficient	h_{sw}	$\frac{1}{0.085 + \frac{1}{2}\sqrt{\frac{\pi}{Pe_L}}} \frac{k_g}{d_p}$	W/m ² /K	[52]
Wall-solid radiative transfer coefficient	h_r	$\frac{\sigma\left(T_s^2 + T_w^2\right)\left(T_s + T_w\right)}{\frac{1}{e_b} + \frac{1}{e_w} - 1}$	W/m ² /K	[50]
Bulk emissivity	e_{b}	$0.5(1+e_p)$	/	[64]
Solid particle emissivity	e_p	0.7	/	[64]
Wall emissivity	$e_{_{w}}$	0.7	/	[64]
Wall-ambient radiative transfer coefficient	h_{rw}	$e_{w}\sigma\left(T_{\rm amb}^{2}+T_{w}^{2}\right)\left(T_{\rm amb}+T_{w}\right)$	W/m ² /K	[54]

References

- [1] Carrillo AJ, González-Aguilar J, Romero M, Coronado JM. Solar Energy on Demand: A Review on High Temperature Thermochemical Heat Storage Systems and Materials. Chem Rev 2019;119:4777–816. https://doi.org/10.1021/acs.chemrev.8b00315.
- [2] Wang B, Li L, Pottas JJ, Bader R, Kreider PB, Wheeler VM, et al. Thermal Model of a Solar Thermochemical Reactor for Metal Oxide Reduction. J Sol Energy Eng 2020;142:1–9. https://doi.org/10.1115/1.4046229.
- [3] Herrmann U, Kearney DW. Survey of Thermal Energy Storage for Parabolic Trough Power Plants. J Sol Energy Eng 2002;124:145–52. https://doi.org/10.1115/1.1467601.
- [4] Gil A, Medrano M, Martorell I, Lazaro A, Dolado P, Zalba B, et al. State of the art on high temperature thermal energy storage for power generation . Part 1 Concepts , materials and modellization. Renew Sustain Energy Rev 2010;14:31–55. https://doi.org/10.1016/j.rser.2009.07.035.
- [5] Bayon A, Carrillo AJ, Mastronardo E, Coronado JM. Chapter Six Thermochemical heat storage at high temperature. Adv Chem Eng 2021;58:247–95. https://doi.org/10.1016/bs.ache.2021.10.004.
- [6] Tregambi C, Troiano M, Montagnaro F, Solimene R, Salatino P. Fluidized Beds for Concentrated Solar Thermal Technologies—A Review. Front Energy Res 2021;618421:1–26. https://doi.org/10.3389/fenrg.2021.618421.
- [7] Wheeler VM, Bader R, Kreider PB, Hangi M, Haussener S, Lipiński W. Modelling of solar thermochemical reaction systems. Sol Energy 2017;156:149–68. https://doi.org/10.1016/j.solener.2017.07.069.
- [8] Pan ZH, Zhao CY. Gas—solid thermochemical heat storage reactors for high-temperature applications. Energy 2017;130:155–73. https://doi.org/10.1016/j.energy.2017.04.102.
- [9] Bayon A, Bader R, Jafarian M, Fedunik-Hofman L, Sun Y, Hinkley J, et al. Technoeconomic assessment of solid–gas thermochemical energy storage systems for solar thermal power applications. Energy 2018;149:473–84. https://doi.org/10.1016/j.energy.2017.11.084.
- [10] Marti J, Haselbacher A, Steinfeld A. A numerical investigation of gas-particle suspensions as heat transfer media for high-temperature concentrated solar power. Int J Heat Mass Transf 2015;90:1056–70. https://doi.org/10.1016/j.ijheatmasstransfer.2015.07.033.

- [11] Urrutia AR, Benoit H, Zambon M, Gauthier D, Flamant G, Mazza G. Simulation of the behavior of a dense SiC particle suspension as an energy transporting vector using computational fluid dynamics (CFD). Chem Eng Res Des 2016;106:141–54. https://doi.org/10.1016/j.cherd.2015.12.008.
- [12] Zhang S, Wang Z. Experimental and numerical investigations on the fluidized heat absorption inside quartz glass and metal tubes. Energies 2019;12:1–21. https://doi.org/10.3390/en12050806.
- [13] van Der Hoef MA, van Sint Annaland M, Kuipers JAM. Computational fluid dynamics for dense gas-solid fluidized beds: A multi-scale modeling strategy. Chem Eng Sci 2004;59:5157–65. https://doi.org/10.1016/j.ces.2004.07.013.
- [14] Wang F, Bai F, Wang Z, Zhang X. Numerical Simulation of Quartz Tube Solid Particle Air Receiver. Energy Procedia 2015;69:573–82. https://doi.org/10.1016/j.egypro.2015.03.066.
- [15] Benoit H, Ansart R, Neau H, Triñanes PG, Flamant G, Simonin O. Three-dimensional numerical simulation of upflow bubbling fluidized bed in opaque tube under high flux solar heating. Am Inst Chem Eng 2018;64:3857–67. https://doi.org/10.1002/aic.16218.
- [16] Li T, Pannala S, Shahnam M. Reprint of "CFD simulations of circulating fluidized bed risers, part II, evaluation of differences between 2D and 3D simulations. Powder Technol 2014;265:13–22. https://doi.org/10.1016/j.powtec.2014.04.007.
- [17] Jackson GS, Imponenti L, Albrecht KJ, Miller DC, Braun RJ. Inert and Reactive Oxide Particles for High-Temperature Thermal Energy Capture and Storage for Concentrating Solar Power. J Sol Energy Eng 2019;141:1–14. https://doi.org/10.1115/1.4042128.
- [18] Meier A, Winkler C, Wuillemin D. Experiment for modelling high temperature rock bed storage. Sol Energy Mater 1991;24:255–64. https://doi.org/10.1016/0165-1633(91)90066-T.
- [19] Mertens N, Alobaid F, Frigge L, Epple B. Dynamic simulation of integrated rock-bed thermocline storage for concentrated solar power. Sol Energy 2014;110:830–42. https://doi.org/10.1016/j.solener.2014.10.021.
- [20] Anderson R, Shiri S, Bindra H, Morris JF. Experimental results and modeling of energy storage and recovery in a packed bed of alumina particles. Appl Energy 2014;119:521–9. https://doi.org/10.1016/j.apenergy.2014.01.030.
- [21] Bayón R, Rojas E. Simulation of thermocline storage for solar thermal power plants: From

- dimensionless results to prototypes and real-size tanks. Int J Heat Mass Transf 2013;60:713–21. https://doi.org/10.1016/j.ijheatmasstransfer.2013.01.047.
- [22] Zanganeh G, Pedretti A, Zavattoni S, Barbato M, Steinfeld A. Packed-bed thermal storage for concentrated solar power Pilot-scale demonstration and industrial-scale design. Sol Energy 2012;86:3084–98. https://doi.org/10.1016/j.solener.2012.07.019.
- [23] Zanganeh G, Pedretti A, Haselbacher A, Steinfeld A. Design of packed bed thermal energy storage systems for high-temperature industrial process heat. Appl Energy 2015;137:812–22. https://doi.org/10.1016/j.apenergy.2014.07.110.
- [24] Preisner NC, Bürger I, Wokon M, Linder M. Numerical investigations of a counter-current moving bed reactor for thermochemical energy storage at high temperatures. Energies 2020;13:1–22. https://doi.org/10.3390/en13030772.
- [25] Wokon M, Block T, Nicolai S, Linder M, Schmücker M. Thermodynamic and kinetic investigation of a technical grade manganese-iron binary oxide for thermochemical energy storage. Sol Energy 2017;153:471–85. https://doi.org/10.1016/j.solener.2017.05.045.
- [26] Wokon M, Kohzer A, Linder M. Investigations on thermochemical energy storage based on technical grade manganese-iron oxide in a lab-scale packed bed reactor. Sol Energy 2017;153:200–14. https://doi.org/10.1016/j.solener.2017.05.034.
- [27] Negri ED, Alfano OM, Chiovetta MG. Moving-Bed Reactor Model for the Direct Reduction of Hematite. Parametric Study. Ind Eng Chem Res 1995;34:4266–76. https://doi.org/10.1021/ie00039a017.
- [28] Valipour MS, Saboohi Y. Numerical investigation of nonisothermal reduction of hematite using Syngas: The shaft scale study. Model Simul Mater Sci Eng 2007;15:487–507. https://doi.org/10.1088/0965-0393/15/5/008.
- [29] Ismail KAR, Stuginsky R. Parametric study on possible fixed bed models for pcm and sensible heat storage. Appl Therm Eng 1999;19:757–88. https://doi.org/10.1016/S1359-4311(98)00081-7.
- [30] Klein P, Roos TH, Sheer TJ. Parametric analysis of a high temperature packed bed thermal storage design for a solar gas turbine. Sol Energy 2015;118:59–73. https://doi.org/10.1016/j.solener.2015.05.008.
- [31] Hamidi M, Wheeler VM, Gao X, Pye J, Catchpole K, Weimer AW. Reduction of iron—manganese oxide particles in a lab-scale packed-bed reactor for thermochemical energy

- storage. Chem Eng Sci 2020;221:1–8. https://doi.org/10.1016/j.ces.2020.115700.
- [32] Lu J, Chen Y, Ding J, Wang W. High temperature energy storage performances of methane reforming with carbon dioxide in a tubular packed reactor. Appl Energy 2016;162:1473–82. https://doi.org/10.1016/j.apenergy.2015.03.140.
- [33] Wang B, Li L, Schäfer F, Pottas JJ, Kumar A, Wheeler VM, et al. Thermal reduction of iron manganese oxide particles in a high-temperature packed-bed solar thermochemical reactor. Chem Eng J 2021;412:1–12. https://doi.org/10.1016/j.cej.2020.128255.
- [34] Schrader AJ, Schieber GL, Ambrosini A, Loutzenhiser PG. Experimental demonstration of a 5 kWth granular-flow reactor for solar thermochemical energy storage with aluminum-doped calcium manganite particles. Appl Therm Eng 2020;173:1–8. https://doi.org/10.1016/j.applthermaleng.2020.115257.
- [35] Schrader AJ, Bush HE, Ranjan D, Loutzenhiser PG. Aluminum-doped calcium manganite particles for solar thermochemical energy storage: Reactor design, particle characterization, and heat and mass transfer modeling. Int J Heat Mass Transf 2020;152:1–15. https://doi.org/10.1016/j.ijheatmasstransfer.2020.119461.
- [36] Yagi J, Szekely J. Mathematical Formulation for the Reduction of Iron Oxide Pellets in Moving Beds With Non-Uniform Gas and Solids Flow. Trans Iron Steel Inst Jpn 1977;17:569–75. https://doi.org/10.2355/isijinternational1966.17.569.
- [37] Yagi J, Szekely J. Computed Results for the Reduction of Iron Oxide Pellets in Moving Beds With Non-Uniform Gas and Solids Flow. Trans Iron Steel Inst Jpn 1977;17:576–85. https://doi.org/10.2355/isijinternational1966.17.576.
- [38] Szekely J. Fluid Flow Phenomena in Metals Processing. 1st ed. Academic Press; 1979. https://doi.org/10.1016/B978-0-12-680840-7.X5001-4.
- [39] Randhir K, Hayes M, Schimmels P, Petrasch J, Klausner J. Synthesis of zero carbon solid-state fuel for long duration energy storage. Joule 2021;submitted.
- [40] Huang W, Korba D, Randhir K, Petrasch J, Klausner J, AuYeung N, et al. Thermochemical reduction modeling in a high-temperature moving-bed reactor for energy storage: 1D model. Appl Energy 2022;306:118009. https://doi.org/10.1016/j.apenergy.2021.118009.
- [41] Nield DA, Bejan A. Convection in Porous Media. Fifth. Springer International Publishing AG; 2017. https://doi.org/10.1007/978-3-319-49562-0.
- [42] Li S, Wheeler VM, Kumar A, Lipiński W. Numerical modelling of ceria undergoing

- reduction in a particle–gas counter-flow: Effects of chemical kinetics under isothermal conditions. Chem Eng Sci 2020;218. https://doi.org/10.1016/j.ces.2020.115553.
- [43] Ergun S. Fluid flow through packed columns. Chem Enfineering Prog 1952;48:88–95. https://doi.org/10.1021/ie50474a011.
- [44] Kränzien PU, Jin Y. Natural Convection in a Two-Dimensional Cell Filled with a Porous Medium: A Direct Numerical Simulation Study. Heat Transf Eng 2018;0:1–10. https://doi.org/10.1080/01457632.2018.1432083.
- [45] Keene DJ, Lipiński W, Davidson JH. The effects of morphology on the thermal reduction of nonstoichiometric ceria. Chem Eng Sci 2014;111:231–43. https://doi.org/10.1016/j.ces.2014.01.010.
- [46] Keene DJ, Davidson JH, Lipiński W. A model of transient heat and mass transfer in a heterogeneous medium of ceria undergoing nonstoichiometric reduction. J Heat Transfer 2013;135:1–9. https://doi.org/10.1115/1.4023494.
- [47] Ströhle S, Haselbacher A, Jovanovic ZR, Steinfeld A. Transient discrete-granule packed-bed reactor model for thermochemical energy storage. Chem Eng Sci 2014;117:465–78. https://doi.org/10.1016/j.ces.2014.07.009.
- [48] Randhir K, King K, Rhodes N, Li L, Hahn D, Mei R, et al. Magnesium-manganese oxides for high temperature thermochemical energy storage. J Energy Storage 2019;21:599–610. https://doi.org/10.1016/j.est.2018.11.024.
- [49] Yang WJ, Zhou ZY, Yu AB. Particle scale studies of heat transfer in a moving bed. Powder Technol 2015;281:99–111. https://doi.org/10.1016/j.powtec.2015.04.071.
- [50] Stenberg V, Sköldberg V, Öhrby L, Rydén M. Evaluation of bed-to-tube surface heat transfer coefficient for a horizontal tube in bubbling fluidized bed at high temperature. Powder Technol 2019;352:488–500. https://doi.org/10.1016/j.powtec.2019.04.073.
- [51] Sullivan, W N, Sabersky, R H. Heat transfer to flowing granular media. Int J Heat Mass Transf 1975;18:97–107. https://doi.org/10.1016/0017-9310(75)90012-5.
- [52] Spelt JK, Brennen CE, Sabersky RH. Heat transfer to flowing granular material. Int J Heat Mass Transf 1982;25:791–6. https://doi.org/10.1016/0017-9310(82)90091-6.
- [53] Miller DC, Pfutzner CJ, Jackson GS. Heat transfer in counterflow fluidized bed of oxide particles for thermal energy storage. Int J Heat Mass Transf 2018;126:730–45. https://doi.org/10.1016/j.ijheatmasstransfer.2018.05.165.

- [54] Li L, Chen C, Singh A, Rahmatian N, AuYeung N, Randhir K, et al. A transient heat transfer model for high temperature solar thermochemical reactors. Int J Hydrogen Energy 2016;41:2307–25. https://doi.org/10.1016/j.ijhydene.2015.11.079.
- [55] Leonard BP. A stable and accurate convective modelling procedure based on quadratic upstream interpolation. Comput Methods Appl Mech Eng 1979;19:59–98. https://doi.org/10.1016/0045-7825(79)90034-3.
- [56] Simoncini V. Computational Methods for Linear Matrix Equations. Soc Ind Appl Math 2016;58:377–441. https://doi.org/10.1137/130912839.
- [57] King K, Randhir K, Klausner J. Calorimetric method for determining the thermochemical energy storage capacities of redox metal oxides. Thermochim Acta 2019;673:105–18. https://doi.org/10.1016/j.tca.2019.01.008.
- [58] Singh AK, Auyeung NJ, Randhir K, Mishra R, Allen KM, Petrasch J, et al. Thermal Reduction of Iron Oxide under Reduced Pressure and Implications on Thermal Conversion E ffi ciency for Solar Thermochemical Fuel Production. Ind Eng Chem Res 2015;54:6793–803. https://doi.org/10.1021/ie504402x.
- [59] Sunarso J, Hashim SS, Zhu N, Zhou W. Perovskite oxides applications in high temperature oxygen separation, solid oxide fuel cell and membrane reactor: A review. Prog Energy Combust Sci 2017;61:57–77. https://doi.org/10.1016/j.pecs.2017.03.003.
- [60] Othmer K. Kirk-Othmer Encyclopedia of Chemical Technology: Fans and Blowers. 5th ed. John Wiley & Sons, Inc.; 2004.
- [61] Wen D, Ding Y. Heat transfer of gas flow through a packed bed. Chem Eng Sci 2006;61:3532–42. https://doi.org/10.1016/j.ces.2005.12.027.
- [62] McDanel Advanced Ceramic Technologies. Alumina Tubes Rods 2015. http://www.mcdanelceramics.com/tubes rods/html.
- [63] MW CJ. Data reported in NIST standard reference database 69. J Phys Chem Ref Data; 2005.
- [64] Sumin Sih S, Barlow JW. The prediction of the emissivity and thermal conductivity of powder beds. Part Sci Technol 2004;22:291–304. https://doi.org/10.1080/02726350490501682a.